저작자표시-비영리-변경금지 **2.0** 대한민국

이용자는 아래의 조건을 따르는 경우에 한하여 자유롭게

- 이 저작물을 복제, 배포, 전송, 전시, 공연 및 방송할 수 있습니다.

다음과 같은 조건을 따라야 합니다:

저작자표시. 귀하는 원저작자를 표시하여야 합니다.

비영리. 귀하는 이 저작물을 영리 목적으로 이용할 수 없습니다.

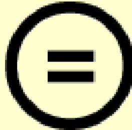
변경금지. 귀하는 이 저작물을 개작, 변형 또는 가공할 수 없습니다.

- 귀하는, 이 저작물의 재이용이나 배포의 경우, 이 저작물에 적용된 이용허락조건을 명확하게 나타내어야 합니다.
- 저작권자로부터 별도의 허가를 받으면 이러한 조건들은 적용되지 않습니다.

저작권법에 따른 이용자의 권리는 위의 내용에 의하여 영향을 받지 않습니다.

이것은 이용허락규약(Legal Code)을 이해하기 쉽게 요약한 것입니다.

Disclaimer

dCollection

Ph.D. DISSERTATION

Low-frequency noise in horizontal floating-gate FET-type gas sensors

수평형 플로팅 게이트 FET형 가스 센서의 저주파 잡음

by

WONJUN SHIN

February 2023

DEPARTMENT OF ELECTRICAL AND COMPUTER ENGINEERING
COLLEGE OF ENGINEERING
SEOUL NATIONAL UNIVERSITY

Low-frequency noise in horizontal floating-gate FET-type gas sensors

수평형 플로팅 게이트 FET형 가스 센서의 저주파 잡음

지도교수 김 재 준

이 논문을 공학박사 학위논문으로 제출함

2023 년 2 월

서울대학교 대학원

전기 · 정보공학부

신 원 준

신원준의 공학박사 학위논문을 인준함

2023 년 2 월

위 원 장 : 장 호 원 (인)

부위원장 : 김 재 준 (인)

위 원 : 이 종 호 (인)

위 원 : 권 혁 인 (인)

위 원 : 최 우 영 (인)

Low-frequency noise in horizontal floating-gate FET-type gas sensors

by

Wonjun Shin

Advisor: Jae-Joon Kim

A dissertation submitted in partial fulfillment of

the requirements for the degree of

Doctor of Philosophy

(Electrical and Computer Engineering)

in Seoul National University

Februrary 2023

Doctoral Committee:

Professor Ho Won Jang, Chair

Professor Jae-Joon Kim, Vice-Chair

Professor Jong-Ho Lee

Professor Hyuck-In Kwon

Associate Professor Woo Young Choi

Acknowledgments

I would like to start by thanking my former doctoral advisor, Prof. Jong-Ho Lee, professor at the Seoul National University and current Minister of Science and ICT. Under his supervision, he allows me to perform cutting-edge research. I spent the best four years of my life with his research group, where I was able to utilize my ability fully. His candid advice on research and academic life has helped me survive as a researcher in a highly competitive research field. I would be grateful to him for shaping my career in ways I never imagined I would be able to achieve. Lastly, let me express my heartfelt gratitude to him for continuing to support my research even after assuming office as the Minister of Science and ICT.

I would also like to thank my doctoral advisor, Prof. Jae-Joon Kim, professor at the Seoul National University. It would have been impossible for me to complete my research on time without Prof. Jae-Joon Kim's guidance, following Professor Jong-Ho Lee's appointment as Minister of Science and ICT.

I would also like to thank Prof. Byung-Gook Park, who was a professor at the Seoul National University. With his extensive knowledge in my subject of study, the professor always provided me with sound advice and constructive ideas. Everyone who knew him was affected by his generosity and warmth. I would like to take this opportunity to express my deepest condolences to Prof. Byung-Gook Park.

I would also like to thank Prof. Ho-Won Jang, professor at the Seoul National University, Prof. Hyuck-In Kwon, professor at the Choong-Ang University, and Prof. Woo Young Choi, professor at the Seoul National University. The professors served on a committee for my doctoral defense and provided valuable insight and advice to my research, which would not have been feasible without them.

Another person whom I should give my gratitude to is Prof. Daewoong Kwon,

professor at the Hanyang University. He assisted me in realizing my research interest in ferroelectric materials and devices. Although outcomes of my research with him were not included in this dissertation, his academic enthusiasm inspired me to push the boundaries of my comprehension and strive for excellence in my research career. I would also like to thank Prof. Jong-Ho Bae, professor at the Kookmin University. He helped me in initiating ferroelectric research and taught me the skills required to study and comprehend semiconductor devices.

Besides, I would like to thank all my former and present co-workers who have helped me, namely, Dr. Seongbin Hong, Dr. Yujeong Jeong, Dr. Gyuweon Jung, and Dr. Dongseok Kwon. Ryun-Han Koo and Jaehyeon Kim, graduate students at the Seoul National University, aided my research with a capability I do not have.

The acknowledgment section cannot be complete without mentioning Radermacher David at the Academy of Korean Studies. He has been the most passionate reader of my research, devoting time and energy to offer inspiration and comments on my thesis.

Lastly, I would like to mention my family, without whom I would not be able to survive a challenging Ph.D. life. My family's unwavering support and dedication provided the strongest foundation for me to overcome any issues or obstacles that came my way.

French philosopher Emmanuel Levinas has claimed that the address of the other constitutes me and that seizure by the other precedes any formation of the self (Judith Butler, "*Giving an Account of Oneself*," Fordham University, New York, 2005). For me, the process of obtaining a doctoral degree was analogous to embodying Levinas' idea. This dissertation was only possible through the relationships and cooperation with people whom I owe my intellectual life to. I would like to extend my gratitude once more to everyone who assisted me during my Ph.D. studies.

The text and figures of this dissertation, in part or in full, are a reprint of the material as it appears in the following journals:

Chapter 2 and 3: Wonjun Shin, Gyuweon Jung, Seongbin Hong, Yujeong Jeong, Jinwoo Park, Dongkyu Jang, Byung-Gook Park, and Jong-Ho Lee, Sens. Actuators B: Chem., vol. 318, p. 128087, Sep. 2020. Reprinted with permission, Copyright © 2020 Elsevier.

Chapter 4: Wonjun Shin, Jaehyeon Kim, Gyuweon Jung, Suyeon Ju, Sung-Ho Park, Yujeong Jeong, Seongbin Hong, Ryun-Han Koo, Yeongheon Yang, Jae-Joon Kim, Seungwu Han, and Jong-Ho Lee, Advanced Science, Jan. 2023, Reprinted with permission, Copyright © 2023 Wiley

Chapter 5: Wonjun Shin, Gyuweon Jung, Seongbin Hong, Yujeong Jeong, Jinwoo Park, Donghee Kim, Dongkyu Jang, Dongseok Kwon, Jong-Ho Bae, Byung-Gook Park, and Jong-Ho Lee, Nanoscale, vol. 12, no. 38, Oct. 2020, Reprinted with permission, Copyright © 2020 RSC; Wonjun Shin, Gyuweon Jung, Seongbin Hong, Yujeong Jeong, Jinwoo Park, Donghee Kim, Byung-Gook Park, and Jong-Ho Lee, Sens. Actuators B: Chem., vol. 357, p. 131398, Apr. 2022. Reprinted with permission, Copyright © 2022 Elsevier.

ABSTRACT

Concerns about indoor and outdoor air quality, industrial gas leaks, and medical diagnostics are driving the demand for high-performance gas sensors. Owing to their structural variety and large surface area, semiconductor-based gas sensors hold great promise. Many earlier reports have successfully obtained a sufficient response and sensitivity to various types of target gases. However, the low-frequency noise (LFN) characteristics of gas sensors have been much less investigated. In this dissertation, LFN characteristics of horizontal floating-gate (FG) field-effect-transistor (HFGFET)-type gas sensors are systematically investigated. The LFN characteristics of the sensors with various sensing materials, including In_2O_3, IGZO, and WO_3, are analyzed. The LFN for the HFGFET-type gas sensors is accurately modeled based on a systematic investigation and on solid physical foundations. It is revealed that the charge fluctuation in both the sensing material and the FET transducer affects the LFN of the sensor. When the LFN of the sensor is determined by the charge fluctuation in the sensing material, LFN spectroscopy can be used to realize selective detection. On the other hand, when the LFN of the FET transducer is determined by the FET transducer, the sensor platform can be used to maximize the SNR. Depending on the application the gas sensor, the LFN should be well controlled, and it is important to have the proper

knowledge to make this engineering possible. This dissertation provides a fundamental foundation on which this can be achieved.

Keywords: horizontal floating-gate field-effect-transistor (HFGFET)-type gas sensor, low-frequency noise (LFN), LFN spectroscopy, signal-to-noise ratio (SNR)

Student number: 2017-20021

CONTENTS

Abstract..i

Contents..iv

List of Figures..viii

List of Tables..xxiii

Chapter 1

Introduction..1

1.1 Study background..1

1.1.1 Gas sensing technology..1

1.1.2 HFGFET-type gas sensors..3

1.1.3 LFN in gas sensors..4

1.2 Purpose of research..7

1.3 Dissertation outline..8

Chapter 2

Fabrication of sensor platform..10

2.1 Sensor Structure..10

2.2 Fabrication process..11

Chapter 3

Comparison of LFN characteristics in sensors with different sensor platforms 14

3.1 Measurement setup..14

3.2 Sensing material characterization..15

3.3 Resistor-type gas sensors..17

3.4 HFGFET-type gas sensors..20

3.5 Quantitative comparison...24

Chapter 4

LFN characteristics of HFGFET-type gas sensors with tungsten oxide sensing layer....................................27

4.1 Sensing material characterization…………..................................27

4.2 LFN characteristics..28

4.3 Selective gas detection via LFN spectroscopy..............................37

Chapter 5

Optimization of signal-to-noise ratio.................................41

5.1 Quantitative evaluation of SNR in gas sensing applications 41

5.2 SNR optimization…………………………………………..,..42

5.2.1 Sensing material characterization…............................43

5.2.2 Comparison of LFN characteristics between resistor- and FET-type gas sensors………………….................................45

5.2.3 Comparison of signal-to-noise ratio between resistor- and FET-type gas sensors ……………………......................50

5.3 Optimization of SNR in HFGFET using transducer and bias condition optimizations..60

5.3.1 Sensing material characterization…..............................60

5.3.2 Comparison of LFN characteristics between the sensors with buried and surface channel FETs..................................61

5.3.3 Comparison of NO_2 gas response between the sensors with buried and surface channel FETs …………….............67

5.3.4 Comparison of signal-to-noise ratio gas response between the sensors with buried and surface channel FETs...69

Chapter 6

Conclusions...75

Bibliography...78

Abstract in Korean..87

List of Publications...89

List of Figures

Figure 2.1. Top SEM image of the resistor-type sensor, HFGFET-type sensor, and HFGFET-type gas sensor with embedded micro-heater. …..……………………..........10

Figure 2.2. Schematic of fabrication process of the resistor- and FET-type gas sensors………………………………………………………...............................12

Figure 3.1. Schematic diagram of H_2S gas response and LFN measurement system. …………………...……..15

Figure 3.2. Top SEM image of In2O3 deposited on (a) Ar and (b) Ar/O_2 mixed ambient conditions. (c) EDS spectrum analysis of In_2O_3 deposited under the Ar ambient conditions. 16

Figure 3.3. (a) Current-voltage (I-V) curves of the resistor-type gas sensors measured at 27°C and 180°C. (b) S_I of the resistor-type gas sensor produced in the Ar/O_2 ambient condition. (c) S_I/I^2 of the resistor-type gas sensors. The inset shows the log-log plot of the R_{SHEET} versus the S_I/I^2 sampled at 40 Hz. (d) S_I/I^2 sampled at

40 Hz and 100 Hz versus the V……………………………………………........18

Figure 3.4. (a) Drain current-CG voltage (I_D-V_{CG}) curves of the FET-type gas sensor measured at 23 and 180 ºC. (b) Drain current-drain-to-source voltage (I_D-V_{DS}) curves measured at 27 ºC. (c) S_{ID} of the FET-type gas sensor at 27 ºC measured in different operating regions. (d) S_{ID}/I_D^2 versus I_D of the FET-type gas sensors and poly Si gate FET used as a sensor platform. (e) Doping concentration versus distance of the FET. ………………………..21

Figure 3.5. Current normalized power spectral densities the resistor- and the FET-type gas sensors. The y_2 axis shows the size normalized results of the sensors....25

Figure 4.1. (a) Top SEM image and (b) GIXRD of the WO_3 thin film, respectively. (c) Wide-scan XPS spectrum, high resolution XPS spectra of (e) O 1s and (f) W, respectively. ...……………………………………………………..................27

Figure 4.2. Drain current-CG voltage (I_D-V_{CG}) curves of a FET-type gas sensor with a WO_3 measured at different temperatures. The open symbols denote the I_D-V_{CG} of

the poly-Si gate FET. (b) S_{ID}/I_D^2 and (c) $f \times S_{ID}/I_D^2$ versus f measured at different V_{CG}s. (d) Change of I_D versus time where Lorentzian-like noise is observed. The I_D amplitude distribution is shown in the inset. (e) Equivalent circuit diagram of the FET-type gas sensor. C_G, C_{ONO}, C_{ox}, and C_P denote the capacitances of the sensing layer, the O/N/O layer, the gate oxide, and the parasitic capacitance, respectively. R_G is the resistance of the sensing material. (f) S_{ID}/I_D^2 sampled at 10 Hz and $(g_m/I_D)^2$ multiplied by a constant versus I_D of the sensor. (g) PIV measurement bias scheme. I_D-V_{CG} and I_D-V_{GS} of the (h-1) FET-type gas sensor and (h-2) poly-Si gate FET measured with DC and PIV measurements as a parameter of t_{on} values, respectively...29

Figure 4.3. (a) Noise-generation mechanism in the HFGFET-type gas sensors. Band structures and corresponding IPR of the electronic states of (b-1) amorphous WO_3 and (b-2) amorphous WO_{3-x}, respectively. The dashed lines indicate the E_F of the materials in each case. (c) Amorphous structure of WO_3. The calculated band structures and corresponding IPR of the electronic states of (d-1) amorphous In_2O_3

and (d-2) amorphous In_2O_{3-x}, respectively. ……………………………..................35

Figure 4.4. (a) S_{ID}/I_D^2 and (b) $f \times S_{ID}/I_D^2$ of the HFGFET-type gas sensors measured at different Ts. (c) S_{ID}/I_D^2 of the poly-Si gate FET versus f measured at different Ts. (d) S_{VG} of the sensors exposed to different gases: Dry air as a reference, NO_2, H_2S, and CO gases for target gases. (e) $\ln(f_c)$ versus $1/k_BT$ of the sensor exposed to different gases: under ambient dry air, NO_2, H_2S, and CO gases. (d) E_a of the dry air, NO_2, CO, H_2S gases..38

Figure 5.1. (a) Deposition rate and (b) R_{SHEET} of the films versus RF power. Top SEM images of In_2O_3 films deposited at RF powers of (c) 50 W, (d) 100 W, and (e) 230 W. ………………………………………………………………………..44

Figure 5.2. Current-voltage (I-V) curves of the resistor-type gas sensors fabricated at different RF sputtering powers. (b) S_I/I^2 of the sensors fabricated at different RF sputtering powers. (c) S_I versus I of the sensor having the In_2O_3 with an RF power of 100 W. (d) S_I/I^2 sampled at 40 Hz versus R_{SHEET}. ……………………..................47

Figure 5.3. (a) Drain current-CG voltage curves of FET-type gas sensor measured at various temperatures. (b) Equivalent circuit of the FET-type gas sensor along the dash-dot line B-B'. (c) S_{ID} versus frequency of the sensor deposited at an RF power of 100 W. The V_{CG} is changed while the V_{DS} is fixed. (d) S_{ID}/I_D^2 versus drain current of FET-type gas sensors……………………………………......................................48

Figure 5.4. (a) ΔI and δI of resistor-type gas sensors versus I deposited at different RF powers. (b) GANRs of the sensors versus RF power. (c) SNR versus I of the sensors versus RF power. (d) Response versus I of the sensors with different RF powers. ………………………………………..…...52

Figure 5.5. (a) g_m and ΔI_D versus I_D of the FET-type gas sensors with different RF powers. (b) ΔV_{FG} versus RF power. (c) δI_D of the sensors versus I_D. (d) SNR, (e) response, and (f) Response×SNR versus I_D of the sensors with different RF powers, respectively. ……………………..54

Figure 5.6. (a) Comparison of SNR between the resistor- and HFGFET-type gas sensors. The upper and lower inserts show the transient gas reaction behavior of

resistor- and FET-type gas sensors under the condition where the SNR of each sensor is largest (100 W for resistor-type gas sensors and 50 W for FET-type gas sensors), respectively. (b) SNR per unit channel area (SNR/μm^2) versus RF power of resistor- and FET-type gas sensors. ……………………………………......................58

Figure 5.7. Drain current-CG voltage (I_D-V_{CG}) and (b) g_m of the sensors with buried and surface channel FETs. The V_{DS} is set at 0.1 and 1.0 V. (c) Transconductance efficiency (g_m/I_D) of the sensors with buried and surface channel FETs versus drain current (I_D). (d) Maximum g_m/I_D of the sensors with buried and surface channel FETs versus T_{chuck}. (e) I_H versus V_H measured by the DC I-V method. (f) T_H versus V_H.…..62

Figure 5.8. (a) S_{ID}/I_D^2 of the sensors with buried and channel FETs versus frequency. (b) S_{ID}/I_D^2 sampled at 10 Hz versus V_{OV} (c) $\sqrt{S_{vg}}$ versus V_{OV} of the sensors with buried and surface channel FETs. …………………….......................................65

Figure 5.9. Response versus V_H of the sensor with buried channel FET. The 500 ppb of NO_2 is exposed to the sensor. (b) Response versus V_{OV} measured at different NO_2

gas concentrations. (c) ΔV_{FG} versus NO_2 gas concentration of the sensor with buried channel FET. The solid and open symbols represent the ΔV_{FG} under dry and humid air ambience, respectively. (d) ΔV_{FG} versus NO_2 gas concentration of the sensors measured at four independent samples. ………………......................................68

Figure 5.10. SNR per unit ΔV_{FG} versus V_{OV} of the sensors calculated at V_{DS} of 0.1 and 1.0 V. (b) Maximum SNR versus V_{DS} of the sensors with different channel structures. (c) g_m versus V_{CG} measured at different V_{DS}s. (d) Optimal V_{OV} where the largest gm and SNR are observed versus V_{DS}……………………..70

Figure 5.12. SNR versus NO_2 gas concentration of the sensors. (b) Evaluated LOD versus f_1 of the sensors. …………………………………………………......72

Chapter 1

Introduction

1.1 Study background

1.1.1 Gas sensor technology

Gas sensing technology offers major contributions to human society via a variety of applications, including environmental monitoring, medical diagnostics, and workplace and public safety maintenance [1]–[3]. Thus, the need for high-performance gas sensor devices and systems has continually grown. To match the growing demand, the worldwide market for gas sensors has developed, with an estimated market value of $1.2B in 2020 that is predicted to reach $2.2B by 2026 [4]. In gas sensing applications, sensors must have a large response and selectivity, high reliability, and low power consumption [5]–[7].

Different types of sensors, such as electrochemical [8], optical [9], and semiconductor-based gas sensors [10], have been suggested. In spite of the optical

gas sensors' rapid reaction and good selectivity for the target gas, the large size and expensive fabrication process make them impractical. Electrochemical gas sensors exhibit good selectivity but have a limited lifespan. Alternatively, semiconductor-based gas sensors are advantageous due to their inexpensive cost, simple fabrication process, and high response [11]. Accordingly, numerous research has been undertaken to enhance the sensing performance of semiconductor-based gas sensors.

In semiconductor-based gas sensors, metal oxides such as tin oxide [12], zinc oxide [13], indium oxide [14], tungsten oxide [15], and indium-zinc-gallium oxide [16], 2D materials such as graphene [17], transition-metal dichalcogenides (TMDCs) [18], black phosphorus [19], and MXene [20], and carbon nanotube (CNT) [21] are used as sensing materials. Numerous research has investigated the gas-sensing characteristics of these materials. In addition, different types of sensor platforms have been suggested to further increase gas-detecting performance [22]. Depending on the sensor platform, the degree to which the chemical interaction between the target gas and sensing material is translated to the sensing signal varies. In addition, it has been reported that the gas-detecting performance could be

improved by optimizing the operating mode of the sensor platform's type. [23].

1.1.2 HFGFET-type gas sensors

Due to their excellent reliability, field effect transistors (FETs) have been widely used as sensor platforms. [11]. Moreover, due to their compatibility with complementary metal-oxide-semiconductor (CMOS), FET-type gas sensors can be integrated with CMOS integrated circuits such as signal conditioning circuitry, multiplexer, and embedded heater, thereby reducing power consumption and enabling further miniaturization. [24]. I. Eisle et al. proposed the FET-type gas sensor with a suspended gate configuration that forms an air gap between the gate and insulator above the channel [25]. However, the fabrication procedure for the suspended gate is difficult, and the air's low dielectric constant results in a low coupling ratio. To boost the coupling ratio, a large sensing area (gate area) is necessary, hence expanding the sensor footprint [26]–[29].

The horizontal floating-gate FET (HFGFET)-type gas sensor has been presented as a sensor platform to the above-mentioned problems [30]. The following is the structure of the HFGFET-type sensor. The FG is protected by a

passivation layer composed of $SiO_2/Si_3N_4/SiO_2$ (O/N/O, 10 nm/20 nm/10 nm), and the CG is formed in an interdigitated pattern with the FG. On the O/N/O layer covering the FG, the interdigitated pattern that will be electrically coupled to the CG and the sensing material is deposited [31], [32]. Consequently, the interdigitated pattern raises the coupling ratio of CG and FG, enhancing the sensing capability [33]–[36]. In addition, because the sensing material is deposited at the last stage of production, the platform is free of any contamination that may have resulted from the deposition of the sensing material [37].

1.1.3 LFN in gas sensors

On the basis of the suggested HFGFET-type gas sensor, a number of sensing materials, including metal oxide, 2D material, and electrolyte, have been investigated to increase the response [30]. Not just in HFGFET-type gas sensors, but in sensor research in general, the emphasis has been on the response. The vast majority of prior research evaluated the response under various conditions, such as changes in operating temperature and humidity level and long-term exposure to ambient gases. In addition, several investigations have concentrated on the

geometric morphologies of sensing materials, such as nanotubes [38], nanodots [39], nanosheets [40], nanowires [41], core-shell nanoparticles [42], and core-shell hollow spheres [43]. However, in the majority of research that examines the limit of detection (LoD) of sensors based on the response, a critical factor has been neglected. In a number of studies, the LoDs of sensors are established by extending the response to the gas concentration at which the value of the response becomes one [44]. However, the noise of the sensing signal also affects the LoD of sensors [45]. Consequently, sensor noise should also be considered while evaluating LoD. In this respect, the signal-to-noise ratio (SNR) is a more relevant figure-of-merit than the response. However, the noise characteristics of gas sensors have only been investigated in a limited number of studies. Even when sensor noise is considered during SNR and LoD analysis, the physical origin of the noise or noise-generating process has not been systematically studied in prior research [46].

Due to the slow sensing speed of semiconductor-based gas sensors, the noise of the sensing signal is dictated by specific forms of low-frequency noise (LFN), such as $1/f$ noise and random telegraph noise (RTN) [47]–[50]. In particular, it is

expected that the LFN will play a greater role in the future design and operation of sensors. There is a growing interest in the fabrication of integrated circuits for intelligent sensing systems[51], [52]. For the widespread integration of sensor arrays into integrated systems, the sensors must be compact and have a high SNR. In highly scaled-down gas sensors, the 1/*f* noise is enlarged inversely proportionate to sensor size [53]–[56]. Consequently, when the sensor is incorporated into an edge device, a greater LFN would significantly reduce the sensor's sensing capability [57]–[59]. Consequently, it is essential to research the LFN of gas sensors thoroughly and to determine the noise-generation process and management strategies [60]. Nevertheless, despite its relevance and importance, the LFN has gotten far less study attention in gas sensor development [61]–[64]. According to Web of Knowledge search results from October 2022, there are a total of 79,420 articles on "gas sensors." Notably, "response" (26,403), "sensitivity" (24,414), and "selectivity" were the most prevalent study topics (10,734). In contrast, only a small number of publications discuss "low-frequency noise" (142) or the "signal-to-noise ratio" (681). The numbers in parentheses indicate the number of articles retrieved

by a search for the terms enclosed in quotation marks. These findings quantitatively indicate the need for LFN research in gas sensing applications.

1.2 Purpose of research

The bulk of research on semiconductor-based gas sensors was devoted to elucidating the gas-detecting process in various sensing materials, including metal oxide [65], graphene [66], and TMDC [67]. These investigations focused on the response, sensitivity, and selectivity of the sensors, regardless of the types of sensing materials they examined. However, no comprehensive study has been conducted on the LFN properties of gas sensors. This dissertation provides a comprehensive investigation of the LFN in semiconductor-based gas sensors, including characterizations of the LFN in resistor-type and HFGFET-type gas sensors, the effects of the process conditions of the sensing materials on the LFN, optimization of the SNR with consideration of the LFN, and LFN spectroscopy for selective detection of the target gas. In this dissertation, the genesis of the LFN in gas sensors and how it can be measured and controlled will be extensively studied.

1.3 Dissertation outline

This dissertation is organized as follows. Chapter 1 outlines the background of the study, providing an introduction to gas sensor technology. In addition, the importance of the sensor platform is demonstrated with a focus on the HFGFET-type gas sensor. Subsequently, the need to investigate the LFN in gas sensors is explained. The purpose of the research and the outline of the dissertation are also introduced. In chapter 2, the structure and fabrication process of the resistor- and HFGFET-type gas sensors are explained. Two different types of sensor platforms are fabricated on the same wafer, making a fair comparison possible. In chapter 3, the LFN characteristics of the resistor-type and HFGFET-type gas sensors with In_2O_3 sensing layer are investigated. Here, the comprehensive comparison of LFN between the HFGFET- and resistor-type gas sensors is examined. Furthermore, the effects of different process conditions of sensing materials on LFN characteristics in each sensor are investigated. In chapter 4, the LFN characteristics of the HFGFET-type gas sensors with WO_3 sensing layer are investigated. Here, the

different noise source in HFGFET-type gas sensor is demonstrated. Chapter 5 proposes a method to evaluate and compare the SNR of gas sensors with resistor- and HFGFET-type gas sensors. Furthermore, the optimization of SNR in each sensor platform is provided. The conclusion of the thesis is presented in Chapter 6.

Chapter 2

Fabrication of sensor platform

2.1 Sensor structure

Using silicon-based CMOS process technology, it is simple to incorporate several types of gas sensors onto the same substrate. In this dissertation, the resistor- and HFGFET-type gas sensors are fabricated on the same wafer, and their properties are rigorously investigated and compared. The structures of resistor- and HFGFET-type gas sensors are depicted as top SEM images in Fig. 2.1(a) and (b), respectively [68]. The resistor-type gas sensors have interdigitated metals as electrodes on which

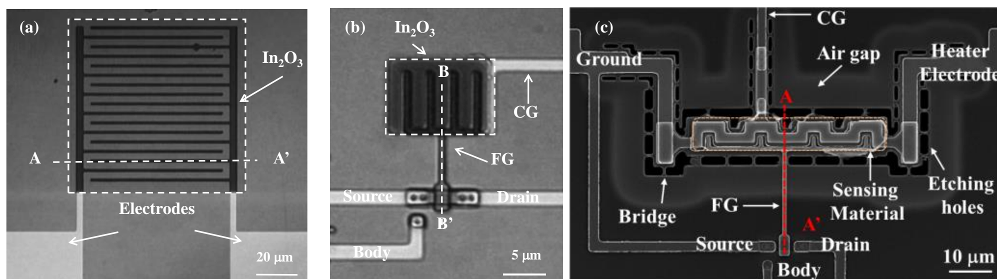

Fig. 2.1. Top SEM image of the resistor-type sensor, HFGFET-type sensor, and HFGFET-type gas sensor with embedded micro-heater

the sensing material is deposited [50]. The size of the resistor-type gas sensor is $100 \times 125\ \mu m^2$ and the distance between the metal electrodes is 2 μm. In the HFGFET-type gas sensors, the CG and FG are horizontally interdigitated from each other, and the sensing layer is formed between the two gates. The embedded micro-heater can be adopted to further improve the sensing characteristics. The top SEM image of the HFGFET-type gas sensor with the micro-heater is shown in Fig. 2(c) . Note that the sensing layer works as a part of the gate. In addition, the O/N/O layer, particularly the N layer, functions as a passivation layer to prevent outside pollutants from entering the FET channel.

2.2 Fabrication process

For a fair comparison, both resistor- and HFGFET-type sensors are fabricated on the same wafer by sharing the manufacturing process steps. Figs. 2.2(a)-(e) depict schematic cross-sectional views of important process phases cut along the dashed lines A-A' and B-B' in Fig. 2.1(a) and (b), respectively. On a 6-inch Si wafer,

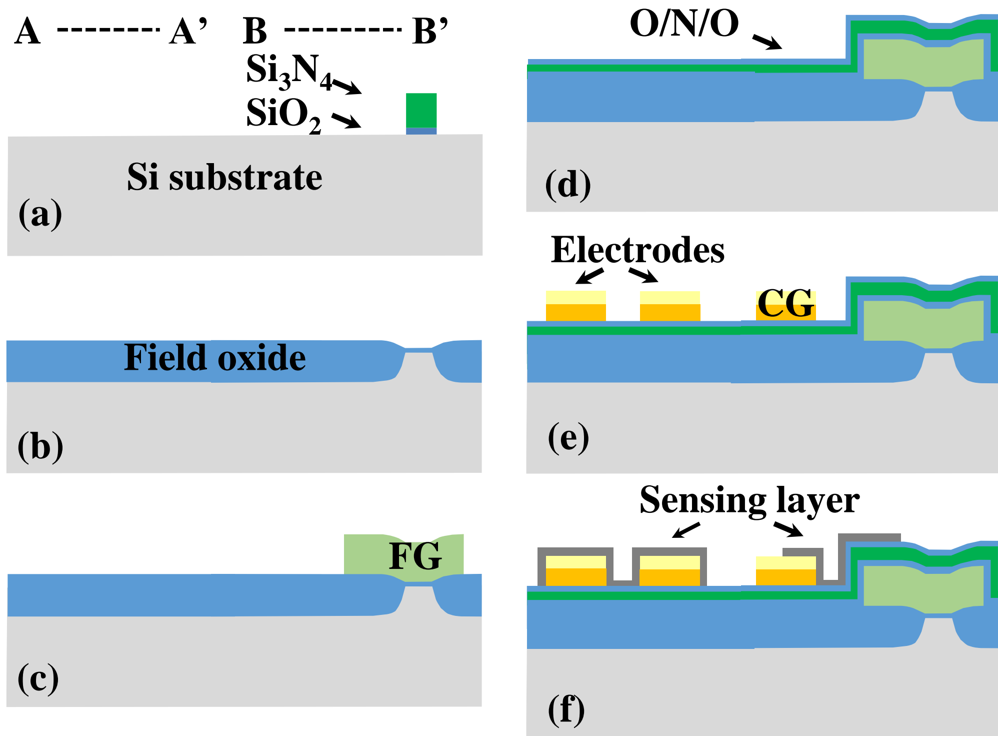

Fig. 2.2. Schematic of the fabrication process of the resistor- and FET-type gas sensors.

the gas sensors are produced utilizing five photomasks and CMOS manufacturing process technology. Patterning a nitride layer generated on the SiO_2 layer (pad oxide) developed on an *n*-type Si substrate defines active areas (a). The nitride is then removed, and a 550-nm-thick oxide is formed (b). The pad oxide is eliminated, and a SiO_2 layer is produced as a sacrifice. After performing ion implantation for

threshold control, the sacrificial layer is eliminated. After developing a 10 nm thick gate oxide, n^+ polycrystalline Si is deposited to generate the FG (or gate electrode for conventional FETs) (c). Then, an O/N/O passivation layer is produced (d). Cr (30 nm) and Au (50 nm) layers are successively produced as the CG, source, and drain electrodes for FET-type gas sensors and electrodes for resistor-type gas sensors after defining contact holes (e). Then, materials for sensing are placed (f). The FG n^+ polysilicon is also used as a micro-heater. Covering this heater is produced beneath the CG in the direction of the multi-fingered FG. To form an air gap underneath the embedded micro-heater, the O/N/O passivation layer, field oxide, and Si substrate are anisotropically and isotropically dry etched, respectively.

Chapter 3

Comparison of LFN characteristics in sensors with different sensor platforms

3.1 Measurement setup and sensing material characterization

Fig. 3.1 depicts a schematic representation of the gas sensing and LFN measuring system. Using a semiconductor parameter analyzer (B1500A) and a probe station with a test chamber, chuck, gas input, and gas exit, the gas-detecting properties of the sensors are evaluated. Target gas is used, and gas flow is regulated by a mass flow controller (MFC). In order to regulate the gas concentration, the target gas is mixed with dry air with a relative humidity of 4% before being introduced into the test chamber. At 180 ^{o}C, the response to H_2S gas molecules is measured. A low noise current amplifier (SR570) and signal analyzer (35670A) are used to assess the LFN power spectral density of the sensors.

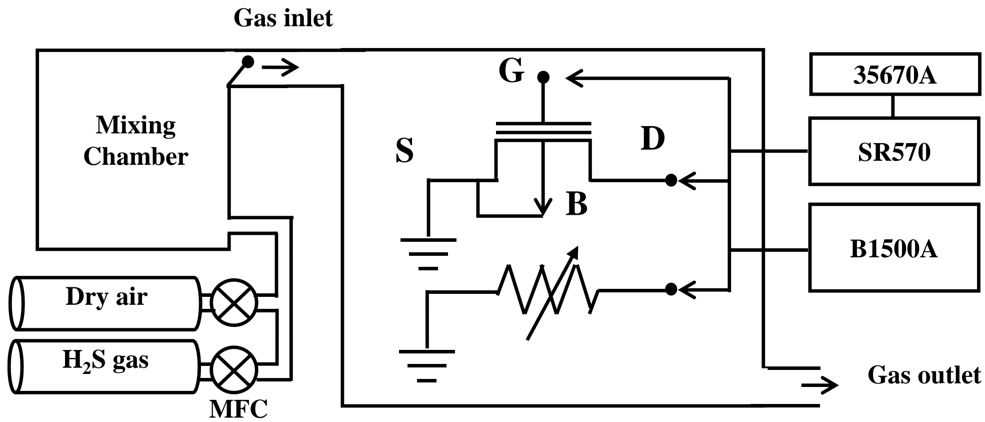

Fig. 3.1. Schematic diagram of H_2S gas response and LFN measurement system.

The SR570 supplies the voltage applied to the electrodes of the resistor-type gas sensor. B1500A and SR570 provide the gate voltage and drain bias of the FET-type gas sensor, respectively. The drain current of the FET-type gas sensor is linked to the SR570, which transforms the current variation into a voltage fluctuation. The 35670A transforms the dynamic signal from the SR570 into a power spectral density.

3.2 Sensing material characterization

Thin films of 12 nm thick In_2O_3 are produced by radio frequency magnetron sputtering using an In_2O_3 target with a purity of 99.99% (4N). The

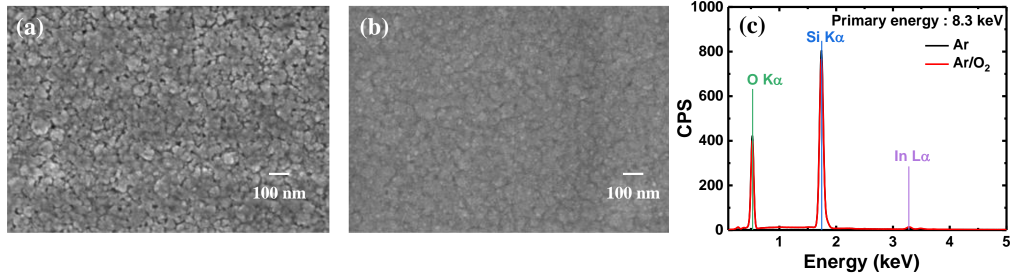

Fig. 3.2. Top SEM image of In_2O_3 deposited on (a) Ar and (b) Ar/O_2 mixed ambient conditions. (c) EDS spectrum analysis of In_2O_3 deposited under the Ar ambient conditions.

substrate temperature is set to 20 ºC, and the sputtering pressure is set at 5 mTorr. The films are deposited in two distinct atmospheres (Ar (30 sccm) and Ar/O_2 (30 sccm/3 sccm) mixed atmosphere) in order to examine the impact of sensing material conditions on the LFN properties. The presence of oxygen molecules in the environment lowers the deposition rate of the sensing material (from 1.1 /s to 0.72 /sec). To stabilize the chemical composition and crystalline structure, the deposited sensing material is subjected to a 100-second heat annealing treatment at 200 ºC. Fig. 3.2(a) and (b) show SEM images of In_2O_3 layers deposited in Ar and Ar/O_2 mixed atmospheres, respectively. Fig. 3.2(c) depicts the Energy Dispersive X-ray Spectroscopy (EDS) examination of the In_2O_3 films.

3.3 Resistor-type gas sensors

Fig. 3.3(a) shows the current-voltage (*I-V*) curves of the resistor-type gas sensor with the In_2O_3 fabricated in the Ar and Ar/O_2 ambient conditions. The curves are measured at 27 and 180 ºC. The conductivity of the resistor-type gas sensor produced in an Ar environment is roughly 10^3 times greater than that produced in an Ar/O_2 atmosphere. When the sensing material is placed in an Ar/O_2 environment, oxygen vacancies that function as a doubly charged donor and provide electrons are decreased [69]. At 180 ºC, the conductivity of a resistor-type gas sensor created in an Ar environment remains unchanged, but the conductivity of a resistor-type gas sensor prepared in an Ar/O_2 atmosphere rises ten times. The larger carrier concentration in the former results in the degeneracy of free carriers, rendering the temperature-independent conductivity of In_2O_3. At 180 ºC, however, the conductivity of the latter material with non-degenerate properties rises owing to a reduction in impurity scattering. Fig. 3.3(b) depicts the S_I of the resistor-type gas

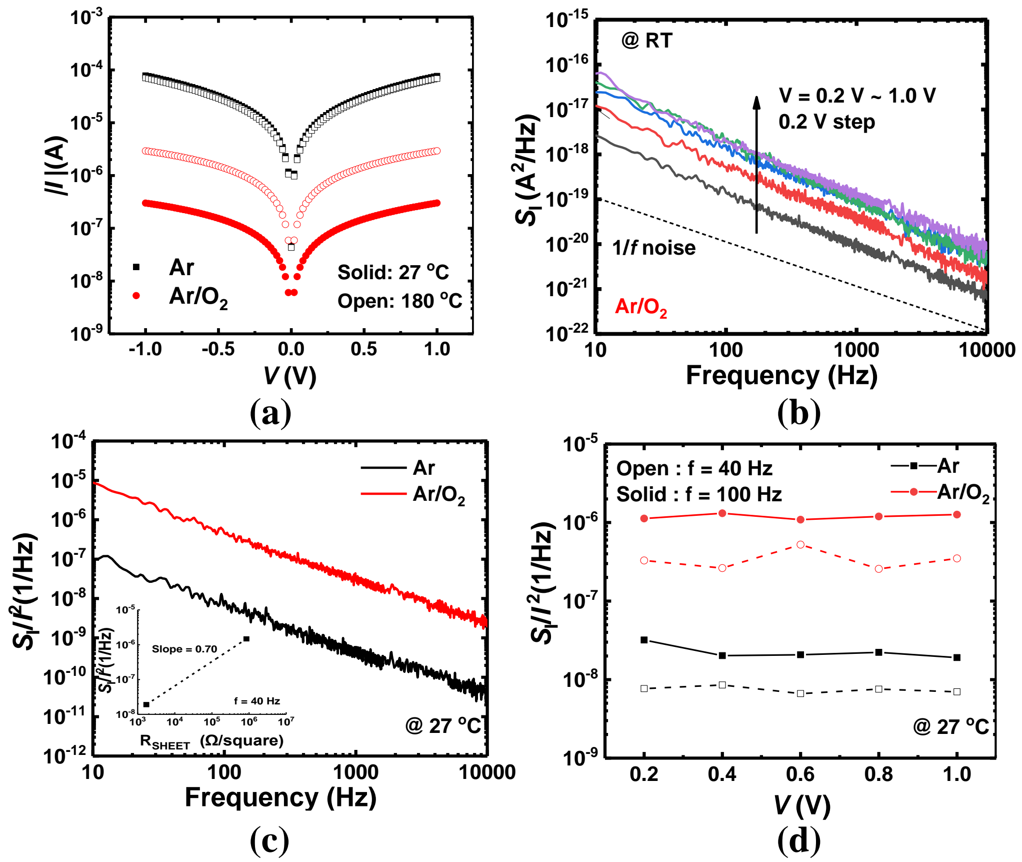

Fig. 3.3. (a) Current-voltage (I-V) curves of the resistor-type gas sensors measured at 27°C and 180°C. (b) S_I of the resistor-type gas sensor produced in the Ar/O_2 ambient condition. (c) S_I/I^2 of the resistor-type gas sensors. The inset shows the log-log plot of the R_{SHEET} versus the S_I/I^2 sampled at 40 Hz. (d) S_I/I^2 sampled at 40 Hz and 100 Hz versus the V.

sensor at various bias circumstances. The V is changed from 0.2 V to 1.0 V in 0.2 V increments). In the low-frequency domain, the behavior of resistor-type gas sensors is 1/f noise [70]–[73]. The LFN of polycrystalline resistors has been

observed to have $1/f$ noise owing to bulk mobility fluctuation (BMF) at the grain boundaries. The grain boundary, which traps carriers and produces the space-charge potential barrier, has a huge number of defects. When the carriers pass over the grain boundaries, the potential barrier arbitrarily obstructs the carrier movement, causing the mobility to vary. The LFN of the polycrystalline resistor is expressed as [74]

$$\frac{S_I}{I^2} = \frac{\alpha_H}{fN}$$

where α_H is the Hooge's parameter and N is the total number of carriers.

The S_I/I^2 of resistor-type gas sensors are shown in Fig. 3.3(c). The magnitude of normalized $1/f$ noise of the resistor-type gas sensor produced in an Ar/O_2 environment is about seventy-five times more than that of the sensor made in an Ar atmosphere. The ratio of the normalized noise to the sheet resistance (R_{SHEET}). The R_{SHEET}s of In_2O_3 deposited in the Ar atmosphere and the Ar/O_2 atmosphere are, correspondingly, 1.7103 Ω/square and 8.5105 Ω /square. The inset of Fig. 3.3(c) shows the R_{SHEET} against the S_I/I^2 at 40 Hz, with a slope of 0.70. The barrier heights of the grain boundaries are obtained by using the following equation

[42].

$$R_{SHEET} = const.\sqrt{T}exp\left(\frac{q\phi_B}{kT}\right).$$

The higher potential barrier height at the grain borders increases the normalized $1/f$ noise. Fig. 3.3(d) shows the S_I/I^2 sampled at 40 Hz and 100 Hz versus V. Note that there is no bias dependency in the normalized noise power spectral densities of resistor-type gas sensors.

3.4 HFGFET-type gas sensors

Fig. 3.4(a) shows drain current-CG voltage (I_D-V_{CG}) curves of the FET-type gas sensor measured at 27 and 180 °C. The off-current is elevated at 180 °C due to leakage current from the source/drain to the substrate junction. Fig. 3.4(b) shows output characteristics (I_D-V_{DS}) curves at 27 °C. Fig. 3.4(c) shows the FET-type gas sensor's S_{ID} measured at 27 °C measured at different operating regions. The $1/f^{\gamma}$ (γ ~ 0.9 to 1.1) characteristic is evident in the FET-type gas sensors. The $1/f$ noise of FETs is generated by either the carrier number fluctuation (CNF) [75] or Hooge's mobility fluctuation (HMF) [45]. The CNF model predicts that $1/f$ noise is produced

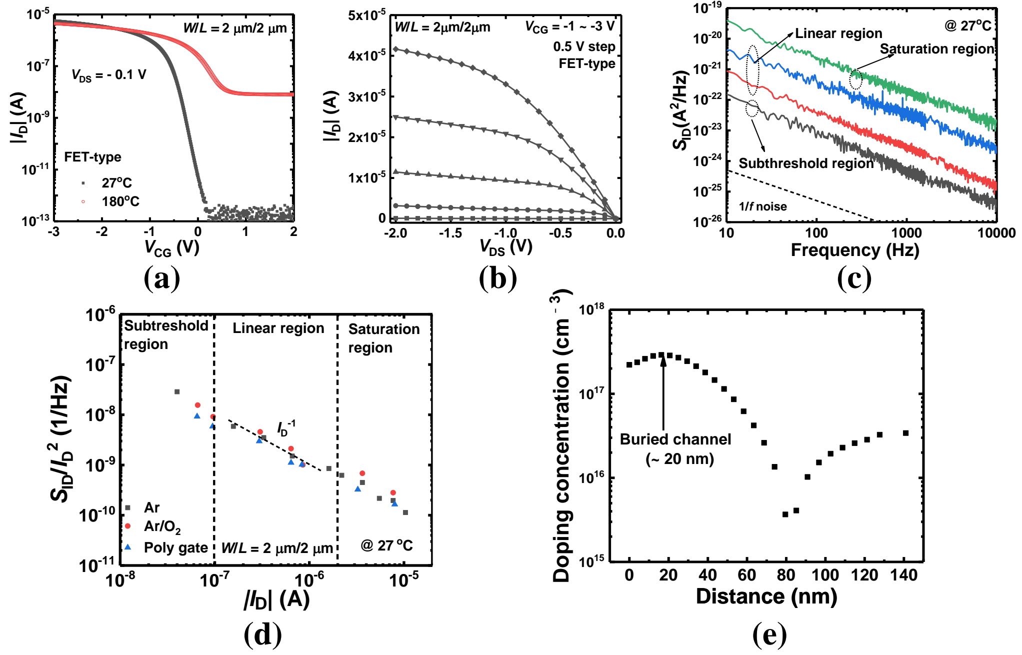

Fig. 3.4. (a) Drain current-CG voltage (I_D-V_{CG}) curves of the FET-type gas sensor measured at 23 and 180 °C. (b) Drain current-drain-to-source voltage (I_D-V_{DS}) curves measured at 27 °C. (c) S_{ID} of the FET-type gas sensor at 27 °C measured in different operating regions. (d) S_{ID}/I_D^2 versus I_D of the FET-type gas sensors and poly-Si gate FET used as a sensor platform. (e) Doping concentration versus distance of the FET.

due to the trapping and detrapping of carriers at the gate oxide/Si channel interface. Each defect has its own time constant, whose value is determined by the distance from the Si/SiO_2 interface. In the low-frequency domain, these defects cause Lorentzian noise due to generation and recombination. A succession of closely

spaced defects results in $1/f$ noise. In the CNF model, the frequency exponent depends on the gate bias due to the energy and location dependence of the trap density. The CNF model is given as [75]

$$\frac{S_{ID}}{{I_D}^2} = (\frac{g_m}{I_D})^2 S_{Vfb}$$

with

$$S_{Vfb} = \frac{q^2 N_t kT\lambda}{WL{C_{Ox}}^2 f}$$

where S_{ID}/I_D^2 is the normalized noise power spectral density of the drain current, S_{Vfb} is the power spectral density of flat band voltage fluctuation, N_t is the volume trap density, λ is the oxide tunneling attenuation distance, and C_{OX} is the gate oxide capacitance per unit area.

In the case where the LFN is generated by the carrier mobility scattering at the bulk of the channel, the behavior of LFN is explained by the HMF model. The carrier mobility is perturbed by scattering centers with variable scattering cross-sections, and the absence of a dominant scattering center causes $1/f$ noise in the low frequency domain. The HMF model is given as [76]

$$\frac{S_{ID}}{{I_D}^2} = \frac{\alpha_H}{fN} = \frac{q\alpha_H}{WLQ_i f} = \frac{\alpha_H \mu_{eff} 2kT}{fL^2 I_D}$$

where Q_i is the inversion charge density per unit area (C/cm^2), μ_{eff} is the effective carrier mobility. Whether the FET follows CNF or HMF model can be determined by the log-log plot of the drain current versus the normalized drain current noise sampled at a fixed frequency.

The S_{ID}/I_D^2 at a fixed frequency changes according to the $(g_m/I_D)^2$ in the plot when the CNF is the dominant noise model. On the other hand, the HMF model shows that the slope of the plot is -1. Fig. 3.4(d) shows that S_{ID}/I_D^2 of 40 Hz decreases with a slope of -1 power of the I_D as the operation region of FET-type gas sensors moves from the subthreshold to the saturation and linear regions. The result shows that HMF is the main LFN-generating mechanism. Here, the legends "Ar" and "Ar/O_2" denote the LFN of FET-type gas sensors with varying sensing material processing conditions. The legend "Poly-gate" denotes the noise characteristics of a *p*-type MOSFET, which is used as a sensor platform. Fig. 3.4(d) depicts the noise characteristics of the *p*-type MOSFET using triangle symbols. The LFN characteristics are almost identical to those of the FET-type gas sensors illustrated

by the circle and square. Note that the *p*-type MOSFET and the HFGFET-type gas sensor are fabricated on the same Si substrate and have identical channel dimensions (W/L = 2 μm/2 μm). The result indicates that the sensing material deposition condition has no effect on the noise of the FET-type gas sensor. The *p*-type MOSFET channel noise determines the LFN properties of a FET-type gas sensor. As seen in Fig. 3.4(e), the TCAD process simulation validates that the channel is generated 20 nm from the gate oxide-Si channel contact, suggesting that the FET-type gas sensors exhibit buried channel properties. As a result, charge fluctuations are mostly caused by scattering in the crystalline silicon bulk rather than trapping/detrapping at the interface.

3.5 Quantitative comparison

In this section, we quantitatively compare the LFN of resistor- and FET-type gas sensors using α_H. The left *y*-axis of Fig. 3.5(a) compares S/I^2 of these sensors. It is observed that the noise of the FET-type sensor is at least ~10 times smaller than that of the resistor-type sensor. The $1/f$ noise of the semiconductor

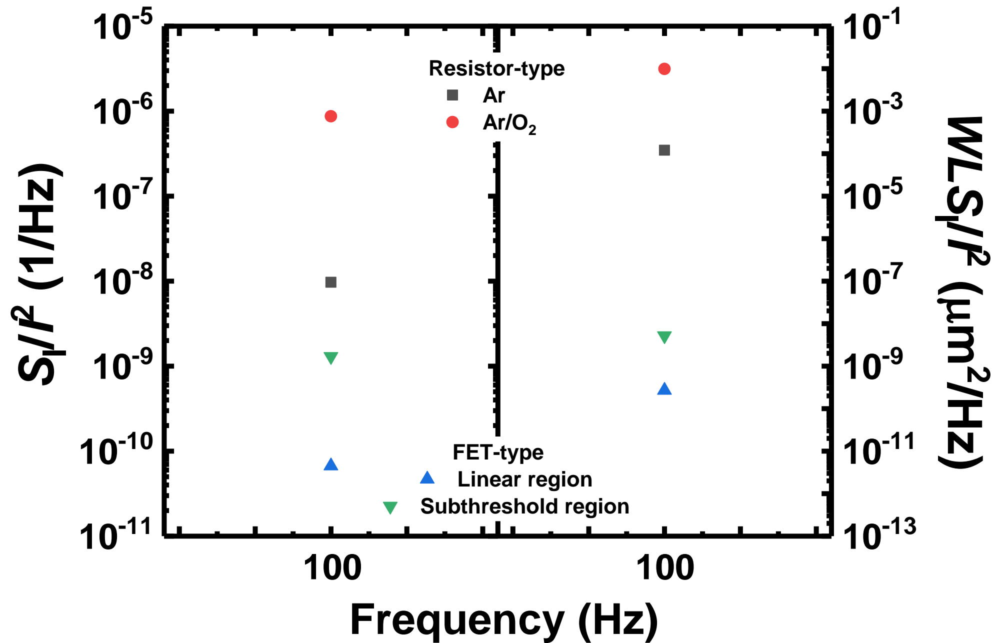

Fig. 3.5. Current normalized power spectral densities the resistor- and the FET-type gas sensors. The y_2 axis shows the size normalized results of the sensors.

device is known to increase as the size of the device decreases, so normalized LFN power spectra should be normalized again with the sizes of the sensors for a fair comparison between the resistor- and the FET-type gas sensors [48]. When comparing the two sensor types, the right y-axis in Fig. 3.5 reveals that the normalized $1/f$ noise of resistor-type gas sensors is at least 10^4 greater than that of FET-type gas sensors. Different conduction characteristics are responsible for the large disparity in normalized $1/f$ noise between the two sensor types. In resistor-

type gas sensors, the polycrystalline In_2O_3 sensing layer serves as the current route, whereas in FET-type gas sensors, the current path is physically isolated from the sensing layer. The LFN of the buried channel structure FET-type gas sensor occurs at the single-crystal Si substrate. Since the magnitude of scatterings in a crystalline structure are much less than in a polycrystalline one, this is a major benefit of the FET-type gas sensors. However, this is not a feature of every FET-based gas sensor. For example, the bottom gate TFT-type gas sensor has a current route in the polycrystalline sensing material because the current passes through the sensing material layer. When TFTs are operating in the subthreshold region, the polycrystalline bulk quality influences device performance, leading to an increase in $1/f$ noise.

Chapter 4

LFN characteristics of HFGFET-type gas sensors with tungsten oxide sensing layer

4.1 Sensing material characterization

At 20 ºC, the sputtering technique is used to deposit an *n*-type semiconducting

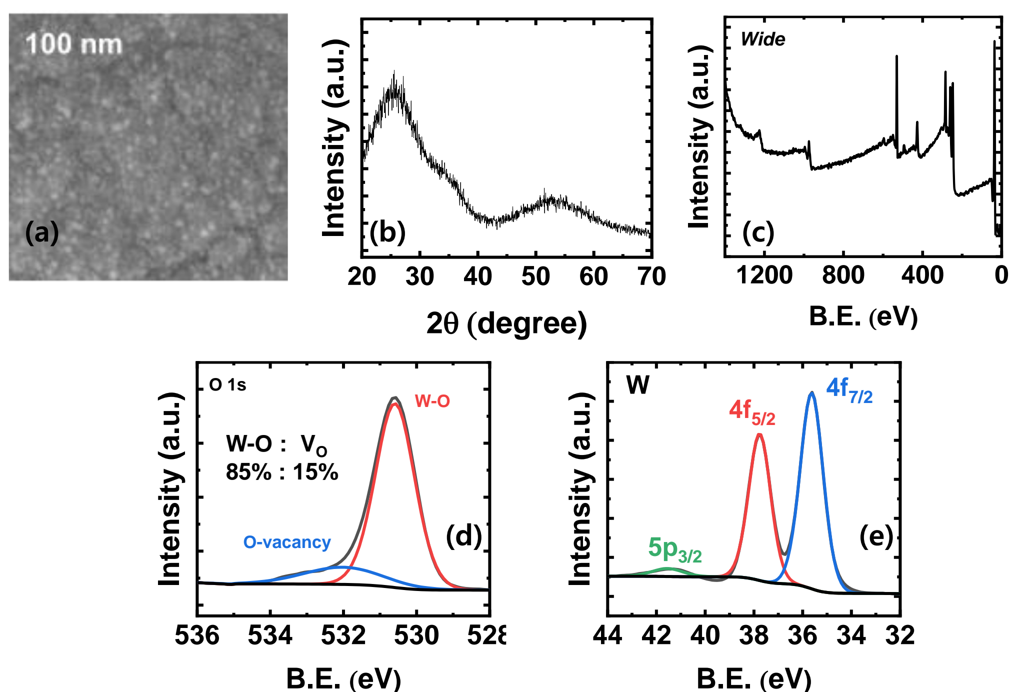

Fig. 4.1. (a) Top SEM image and (b) GIXRD of the WO3 thin film, respectively. (c) Wide-scan XPS spectrum, high resolution XPS spectra of (e) O 1s and (f) W, respectively.

WO_3 that is 20 nm thick. Fig. 4.1(a) and (b), correspondingly, show a top SEM image and the grazing incidence X-ray diffraction analysis (GIXRD) of WO_3 deposited between the CG and FG [77]. These results demonstrate the deposited film is amorphous. Fig. 4.1(c), (d), and (e), correspondingly, displays the wide-scan and high-resolution X-ray photoelectron spectroscopy (XPS) spectra of O 1s and W 4f, respectively. The W:O composition ratio is 1:3 in a quantitative study based on the spectral area.

4.2 LFN characteristics

The transfer characteristics of the HFGFET-type gas sensor with a WO_3 sensing layer as a parameter of T are shown in Fig. 4.2(a). The sensor exhibits conventional p-type FET properties, with a subthreshold swing (SS) of 90 mV at 27 °C and a threshold voltage (V_{th}) of 0.28 V. The curves for the poly-Si gate FET that served as the sensor platform were measured at 27 °C and are shown by open symbols. Due to the different work functions of poly-Si and WO_3, the sensor with WO_3 has

a lower V_{th} than a poly-Si gate FET.

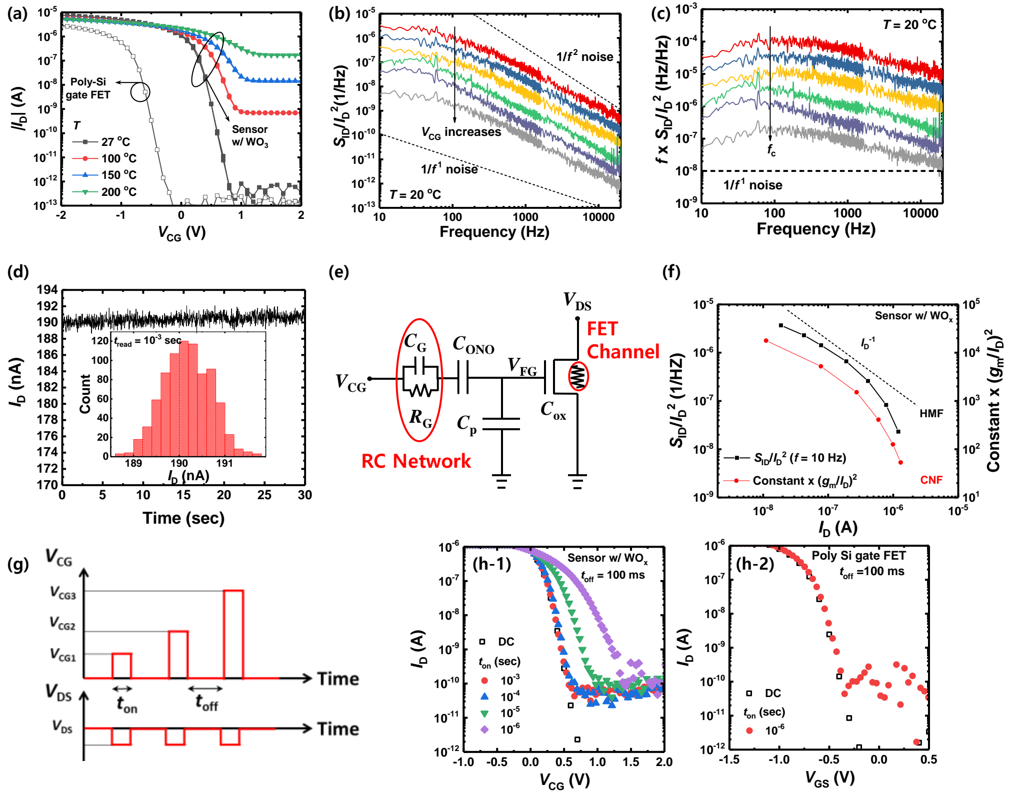

Fig. 4.2. (a) I_D-V_{CG} curves of a FET-type gas sensor with a WO_3 measured at different temperatures. The open symbols denote the I_D-V_{CG} of the poly-Si gate FET. (b) S_{ID}/I_D^2 and (c) $f \times S_{ID}/I_D^2$ versus f measured at different V_{CG}s. (d) The I_D amplitude distribution is shown in the inset. (e) Equivalent circuit diagram of the FET-type gas sensor. (f) S_{ID}/I_D^2 sampled at 10 Hz and $(g_m/I_D)^2$ multiplied by a constant versus I_D of the sensor. (g) PIV measurement bias scheme. I_D-V_{CG} and I_D-V_{GS} of the (h-1) FET-type gas sensor and (h-2) poly-Si gate FET measured with DC and PIV measurements as a parameter of t_{on} values, respectively.

The S_{ID}/I_D^2s under various bias settings are shown in Fig. 4.2(b) as a function of frequency (f). V_{CG} increases from -0.5 V to 0.5 V, while V_{DS} is set at -0.1 V. Fig. 4.2(c) depicts the Lorentzian curve with a corner frequency (f_c) at f = 100 Hz for the FET-type gas sensor with the WO_3 sensing layer. The main source of Lorentzian noise is random telegraph noise (RTN), which is produced when carriers in a FET channel are trapped or released from traps within a gate oxide. However, RTN is unable to account for the Lorentzian noise behavior of the HFGFET-type gas sensor. The reason for this is as follows: 1) The *p*-type FET in the FET transducer features a buried channel structure, with the conductive channel forming around 20 nm away from the gate oxide. The behavior of S_{ID}/I_D^2 in the FET transducer differs from that of $(g_m/I_D)^2$ with respect to I_D, demonstrating that the poly-Si gate FET's LFN properties are independent of the CNF. Therefore, it is unlikely that the process of carriers being trapped in or released from oxide traps would be the primary factor affecting the sensor's overall LFN properties. 2) The gate bias has a significant impact on the kinetics of the trapping and detrapping process, and as a result, f_c exhibits bias dependency if the RTN is the main reason for the Lorentzian-like noise

[78]. But when V_{CG} rises, the f_c of the FET-type gas sensor remains constant. In addition, the fluctuation of I_D over time under the bias condition where the Lorentzian-like noise is seen is shown in Fig. 4.2(d). The related I_D amplitude distribution (Inset of Figure 4.2(d)) confirms that I_D does not exhibit discrete current fluctuations in this instance, but I_D has a Gaussian distribution. These results confirm that the Lorentzian-like noise is not generated from the RTN.

The sensing material deposited between the CG and FG in FET-type gas sensors may also be taken into account as a potential noise source. A FET-type gas sensor's equivalent circuit design is shown in Fig. 4.2(e). The capacitances of the sensing layer, the O/N/O layer, the gate oxide, and the parasitic capacitance are denoted as C_G, C_{ONO}, C_{ox}, and C_P, respectively. The sensing material's resistance is R_G. The voltage coupled between the CG and FG changes when there are charge fluctuations in the sensing material, which in turn causes I_D to vary. The charge fluctuation in the sensing material comes from two sources: 1) Variation in the adsorbed gas's number; and 2) Variation in charge as a result of carrier exchange between the sensing material and the adsorbed gas molecules.

1) First, we consider the number fluctuation of the adsorbed gas, the behavior of which can be understood with an analogy of the generation-recombination (G-R) [49]. By using the same method as for the G-R noise, it is possible to obtain the PSD of the gate voltage caused by adsorption and desorption. The PSD has a very low f_c, however, since gas molecules adsorb to and desorb from the sensing material at a very slow rate. According to the previous study, f_c typically has a value of 10^{-2} Hz [79]. As a result, it is not plausible to reconcile the adsorption/desorption noise of gas molecules with the LFN characteristics of the HFGFET-type gas sensors.

2) The charge fluctuation caused by the carrier exchange between the molecules that have been adsorbed and the sensing material must also be taken into account. A local diffusion current is created during the carrier exchange process.

$$\overline{\Delta I_{g,sensing2}}^{2} = \frac{4kT}{R_G}. \quad (3)$$

Fig. 4.2(e) demonstrates the existence of a parallel combination of R_G and C_G-based resistor-capacitor (RC) network in the sensing material. The transfer function of the RC network may convert the local current noise to voltage noise. The transfer function is expressed as

$$H(s) = \frac{1}{1+sR_GC_{eq}} \quad (4)$$

where

$$C_{eq} = C_G + C_p + C_{ONO.} \quad (5)$$

Thus, the voltage noise PSD ($\overline{\Delta V_{g,sensing2}{}^2}$) is given by

$$\overline{\Delta V_{g,sensing2}{}^2}(f) = |H(s)|^2\overline{\Delta I_{g,sensing2}{}^2} = \frac{4kTR_G}{1+(2\pi R_GC_{eq}f)^2}. \quad (6)$$

Accordingly, $\overline{\Delta V_{g,sensing2}{}^2}$ has the shape of a low-pass filter with a corner frequency ($f_{c,2}$) of $1/R_GC_{eq}$. When $\overline{\Delta V_{g,sensing}{}^2}(f)$ is reflected in the drain current fluctuation, its amplitude is multiplied by g_m^2. When the drain current variation reflects $\overline{\Delta V_{g,sensing}{}^2}(f)$, its amplitude is amplified by g_m^2. Fig. 4.2(f) shows S_{ID}/I_D^2 sampled at 10 Hz and $(g_m/I_D)^2$ multiplied by the constant versus I_D of the sensor. Here, S_{ID}/I_D^2 and $(g_m/I_D)^2$ show the same behavior with respect to I_D, verifying that Equation 8 is well fitted to the noise of the sensor. The fact that S_{ID}'s magnitude is greater than the FET intrinsic $1/f$ noise is what causes the Lorentzian-like noise. As shown in Fig. 4.2(b), the magnitude of measured S_{ID}/I_D^2 is substantially bigger than the $S_{ID,FET}/I_{D,FET}^2$.

We perform pulsed I-V (PIV) measurements of the FET-type gas sensor and

contrast these results with those of a poly-Si gate FET to confirm the presence of the RC network in the sensing material area. The biasing scheme used for the PIV measurement is shown in Fig. 4.2(g). The I_D-V_{CG} of the FET-type gas sensor is shown in Fig. 4.2(h-1), together with DC and pulsed I-V (PIV) readings at different t_{on} values. The PIV measurement yields a substantially bigger off-current value for the FET-type gas sensor than does the DC measurement. This is a result of the WGFMU module's lower limit in the present measurement (100 pA). The RC delay in the sensing material causes the *SS* to increase with a drop in t_{on}. The findings of the LFN measurement are consistent with the delay in the I_D-V_{GS} curves seen by PIV. As demonstrated in Fig. 4.2(h-2), the poly-Si gate FET does not exhibit a rise in *SS*, in contrast to the FET-type gas sensor, even at a t_{on} value of 10^{-6} s.

Here, it's crucial to explain why, in contrast to indium oxide, the noise created in the WO_3 is higher than that in the FET channel. Please note that LFN characteristics of HFGFET-type gas sensors using In_2O_3 were shown in Chapter 3;

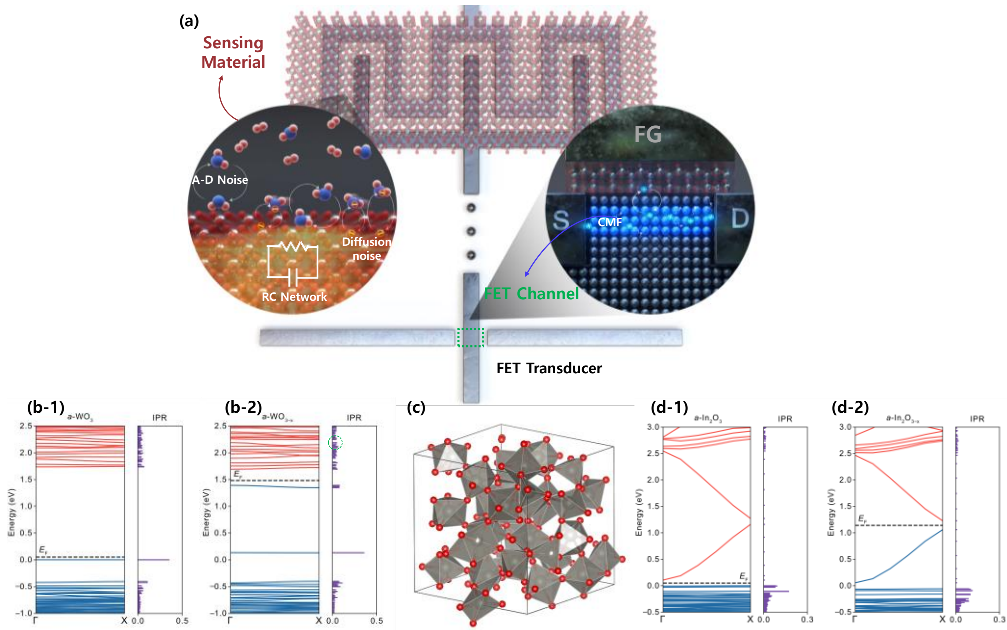

Fig. 4.3. (a) Noise-generation mechanism in the HFGFET-type gas sensors. Band structures and corresponding IPR of the electronic states of (b-1) amorphous WO_3 and (b-2) amorphous WO_{3-x}, respectively. The dashed lines indicate the E_F of the materials in each case. (c) Amorphous structure of WO_3. The calculated band structures and corresponding IPR of the electronic states of (d-1) amorphous In_2O_3 and (d-2) amorphous In_2O_{3-x}, respectively.

the FET transducer determines the noise of the sensor. Such different LFN characteristics are caused by the RC network in the sensing materials. The resistance of a reducible metal oxide varies greatly depending on the energy level of the oxygen vacancy. Oxygen vacancies serve as an electron donors and boost the conductivity of *n*-type metal oxides [69]. In order to verify the properties of

oxygen vacancy in WO_3, a DFT analysis is conducted. The computed band structure and inverse participation ratio (IPR) of the electrical structure of amorphous WO_3 and WO_{3-x}, respectively, are shown in Fig. 4.3(b-1) and (b-2). Fig. 4.3(c) shows the comparable amorphous WO_3. The valence band maximum (VBM) and conduction band minimum (CBM) show minor dispersions in WO_3 and WO_{3-x}. The states are also localized, as seen by the high IPR value. High IPR values may be seen close to the CBM even when there is an oxygen vacancy. The clustered IPR shown by the dashed circle in Fig. 4.3(b-2) confirms that the oxygen vacancies in WO_3 function as a deep donor. No matter how amorphous the structure or where the oxygen vacancy is located, WO_3's oxygen vacancy functions as a deep donor.

The ideal material condition appropriate for LFN spectroscopy is given based on these findings. On the one hand, the LFN of the sensor is governed by the FET channel when the resistance of the metal oxide is too low (such as in In_2O_3). It is difficult to employ LFN as a sensing feature for selective detection in this situation because the LFN of the sensor is the same regardless of the gas response. On the other hand, if the resistance is too high, the f_c will be too small, which will take a

long time to acquire and will delay the detection of the target gas. Therefore, it's crucial to choose a sensing material with a resistance value that's neither too high nor too low. According to this viewpoint, the best material for selective detection in FET-type gas sensors is WO_3 with a deep level oxygen vacancy.

4.3 Selective gas detection via LFN spectroscopy

In this section, we demonstrate how the gas response affects the LFN properties of the FET-type gas sensor. Because the sensing material determines the LFN characteristics of the FET-type gas sensor using WO_3, exposure to various target gases will result in distinct LFN characteristics, which may be used to assess the selectivity of the sensor. A T value greater than 100 °C is often necessary for metal oxide sensing materials to interact with the target gases. In light of this, the impacts of T on the sensors' LFN properties are examined. The validity of the noise

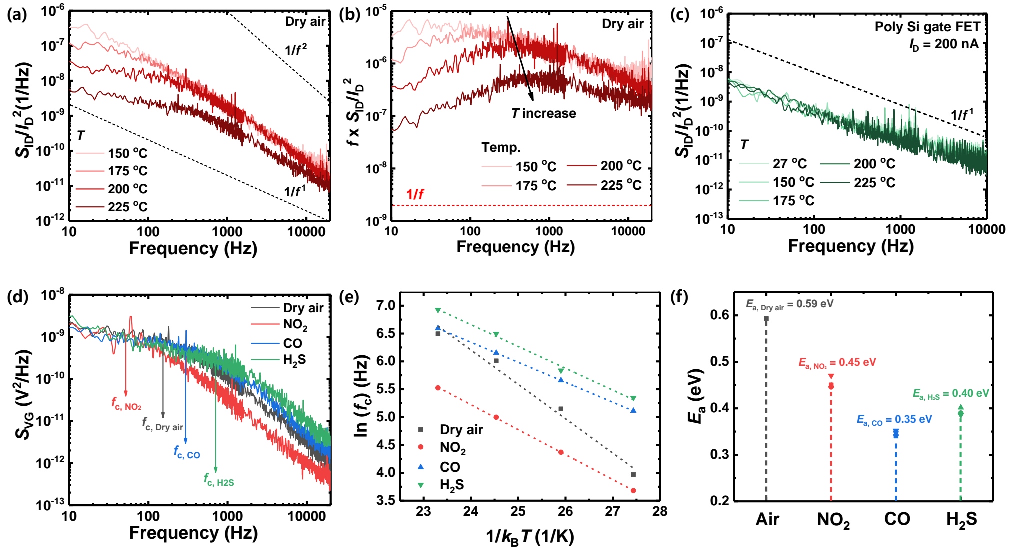

Fig. 4.4. (a) S_{ID}/I_D^2 and (b) $f \times S_{ID}/I_D^2$ of the HFGFET-type gas sensors measured at different Ts. (c) S_{ID}/I_D^2 of the poly-Si gate FET versus f measured at different Ts. (d) S_{VG} of the sensors exposed to different gases: Dry air as a reference, NO_2, H_2S, and CO gases for target gases. (e) ln(f_c) versus $1/k_BT$ of the sensor exposed to different gases: under ambient dry air, NO_2, H_2S, and CO gases. (d) E_a of the dry air, NO_2, CO, H_2S gases.

model is confirmed by examining the impacts of T. The S_{ID}/I_D^2 of the FET-type gas sensor is shown as a parameter of T in Fig. 4.4(a). A 400 nA of I_D value was used to measure the PSDs. Plotted in Fig. 4.4(b) is S_{ID}/I_D^2multiplied by frequency versus frequency.

With rising T, the maximum value of $f \times S_{ID}/I_D^2$, which corresponds to the f_c,

moves to a higher frequency. The reduction in R_G with increasing T may be used to explain the rise in the f_c. Due to an increase in carrier concentration and a drop in potential barrier height at the grain boundaries, the resistance in semiconducting metal oxide decreases as T increases. The S_{ID}/I_D^2 of the poly-Si gate FET is shown against f as a parameter of T in Fig. 4.4(c). The poly-Si gate FET exhibits $1/f$ noise behavior regardless of how T varies, in contrast to the FET-type gas sensors. These findings further show that the sensing medium, not the FET transducer, determines the LFN properties of the sensor.

The S_{VG} of a FET-type gas sensor is shown in Fig. 4.4(d) under various environmental circumstances, including dry air as a reference and NO_2, H_2S, and CO. At 200 °C, the PSDs are measured. A change in f_c that can be readily seen when the sensor is exposed to several target gases may be exploited as a characteristic sensing feature to achieve selective detection. This happens because the RC network and, therefore, f_c vary when WO_3 is exposed to various gases. The noise activation energy (E_a) is determined from the slope of the Arrhenius plot ($\ln(f_c)$ vs $1/k_BT$) in Fig. 4.4(e) since the characteristic time exponentially varies on T. Different

E_a values for various gases emerge from the gas sensing kinetics' influence on the characteristic time of the charge fluctuation. Figure 4.4(f) displays the E_a value for each target gas, which was calculated from the slope of the curve between f_c and $1/k_{BT}$.

For each target gas, the E_as are extracted at four distinct gas concentrations. The E_a values of each of the target gases are the same regardless of the change in gas concentration, proving the efficacy of LFN spectroscopy for selective detection. For the gases O_2, NO_2, CO, and H_2S, the E_a values calculated from the Arrhenius plot are 0.59, 0.45, 0.35, and 0.40 eV, respectively. The target gases are easily separated since the E_a values are easily distinct. Noise spectroscopy provides a significant advantage over traditional sensor technology in that selective detection is accomplished with a single sensor without using a dense array of sensors.

Chapter 5

Optimization of signal-to-noise ratio

5.1 Quantitative evaluation of SNR in gas sensing applications

Until far, research on gas sensors has mostly focused on increasing the magnitudes of the response of different sensing materials, as well as the sensor platforms and measurement conditions. However, one must determine the lowest observable signal that a sensor can accurately detect to assess the LoD of sensors. It is significant to highlight that the noise of the sensor determines the smallest change that can be resolved. The noise sources of sensors can be measured, characterized, and predicted using an analysis of the LFN. So, while assessing the LoD and choosing the ideal manufacturing and operating conditions, the LFN must be considered. As a result, the SNR, which also incorporates the LFN, is a more reliable measure for assessing the LoD than the response, which only takes the signal's size into consideration. A signal-to-noise ratio (SNR) of at least three is

required in order to be deemed meaningful, as per IUPAC regulations [80]. The SNR is defined as

$$\mathrm{SNR} = \frac{\Delta I}{\delta I} = \frac{I_g - I_a}{\sqrt{\int_{f1}^{f2} S_I(f)df}} = \frac{I_g - I_a}{\sqrt{BW} \times \sqrt{S_I(f=1Hz)}}$$

where ΔI is the signal generated from the gas reaction; δI is the root-mean-square noise amplitude; I_g and I_a are the currents of the sensor after and before the gas reaction, respectively; S_I (f = 1 Hz) is PSD of the current noise at a frequency of 1 Hz; and BW is a bandwidth-related term that depends on the largest (f_2) and smallest (f_1) frequencies sampled; $BW = \ln(f_2/f_1)$. Note that $\sqrt{BW}$ ranges from about 3.5 to 3.8 in typical gas sensing measurements. The amplitude of the 1/*f* noise is many orders bigger than the thermal noise in the observed BW range; hence the LFN decides the δI. In order to accurately predict a lower bound on the sensor's detection limit, an estimate of the SNR must be based on a precise measurement of the PSD of 1/*f* noise.

5.2 SNR optimization

5.2.1 Sensing material characterization

Due to its low noise characteristics, In_2O_3 is employed as a sensing material and deposited under various circumstances to improve the SNR of HFGFET-type gas sensors. In order to confirm the advantage of HFGFET-type gas sensors in terms of SNR, the SNR of the sensor is compared to that of the resistor-type gas sensors.

By employing an In_2O_3 target (99.99% (4N)) and an RF magnetron, 30 nm of In_2O_3 thin films are deposited. At 30 sccm, 20 ºC, and 5 mTorr, respectively, the argon flow rate, substrate temperature, and sputtering pressure are all established. In_2O_3 films are fabricated at different RF powers (50, 70, 100, 150, and 230 W). The deposition rate of In_2O_3 film rises from 28.8 to 144 /min with an increase in RF power, as shown in Fig. 5.1(a) [81]. Higher RF power increases the plasma's argon ion content and the target's bombardment. As a result, the rate of deposition rises along with the number of atoms blasted from the In_2O_3 target. Fig. 5.1(b) shows

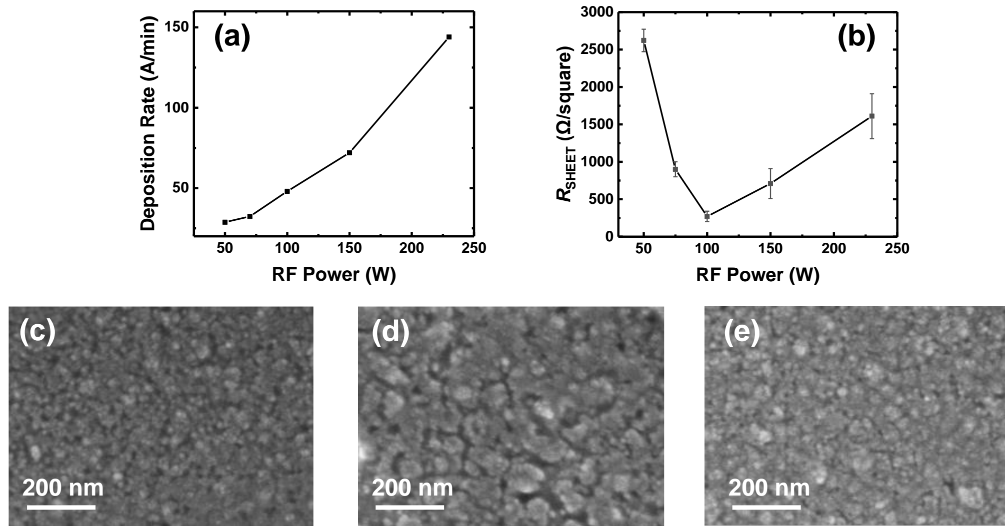

Fig. 5.1. (a) Deposition rate and (b) R_{SHEET} of the films versus RF power. Top SEM images of In_2O_3 films deposited at RF powers of (c) 50 W, (d) 100 W, and (e) 230 W.

sheet resistances (R_{SHEET}s) of the films prepared at various RF power. The R_{SHEET}s of In_2O_3 films decrease as RF power increases when fabricated at low RF powers (50, 70, and 100 W). The In_2O_3 film's grain size enlarges as the RF power rises because the ion cluster energy increases prior to their collision with the substrate. As a result, there are fewer grain boundaries, which reduces the dispersion of charge carriers at the grain borders and raises the conductivity of the film. However, when In_2O_3 films are deposited using high RF power (150 and 230 W), the R_{SHEET} of the In_2O_3 film rises. It seems that an excessive RF power supply causes the In_2O_3 film

to have a high defect density and smaller grain size. The R_{SHEET} of In_2O_3 films rises when carriers scatter at more grain boundaries. Additionally, the homogeneity of the In_2O_3 film is worse when it is deposited at high RF energies than when it is deposited at low RF values. The top SEM images of In_2O_3 films deposited at various RF powers are shown in Fig. 5.1(c)-(e).

5.2.2 Comparison of LFN characteristics between resistor- and HFGFET-type gas sensors

The resistor-type gas sensors' transfer characteristics (I-V), as measured at 27 °C, are shown in Fig. 5.2(a). The resistor-type gas sensor's conductivity increases as the RF power used to deposit In_2O_3 layer rises from 50 to 70 and 100 W. The conductivity then declines as the RF power rises from 100 to 150 and 230 W. In_2O_3 sensing layer resistor-type gas sensors with normalized LFN power spectra (S_I/I^2) that were deposited at various RF powers are shown in Fig. 5.2(b). Gas sensors made of resistors exhibit $1/f$ noise behavior. Fig. 5.2(c) exhibits the S_I versus I of the sensor deposited at 100 W. It is feasible to compare the LFN characteristics of the sensors with In_2O_3 prepared at various RF powers because the noise power is

proportional to the I^2. $1/f$ noise behavior in poly-Si originates from the carrier mobility fluctuation (CMF) at the grain boundaries. Fig. 5.2(d) shows a S_I/I^2 sampled at 40 Hz versus R_{SHEET} of resistor-type gas sensors. The outcome is separated into two groups based on two distinct slopes of 100 W. The S_I/I^2 diminishes proportionately to R_{SHEET} when the sensing material is deposited at low RF power. On the other hand, sensors with sensing material deposited at high RF power exhibit an increase in normalized noise that is proportional to R_{SHEET}^2. The proportionality of the normalized noise to R_{SHEET} or R_{SHEET}^2 is used to determine whether the LFN comes from the bulk or the interface for homogeneous metals and semiconductors [82]. The result shows that at an RF power of around 100 W, the origin of the $1/f$ noise changes from the bulk of the sensing material to the interface

between the sensing material and the O/N/O layer. The bulk quality of the In_2O_3 film affects the LFN properties of resistor-type gas sensors with low RF power sensing layer deposition. The CMF at the grain boundary grows as the In_2O_3 film's

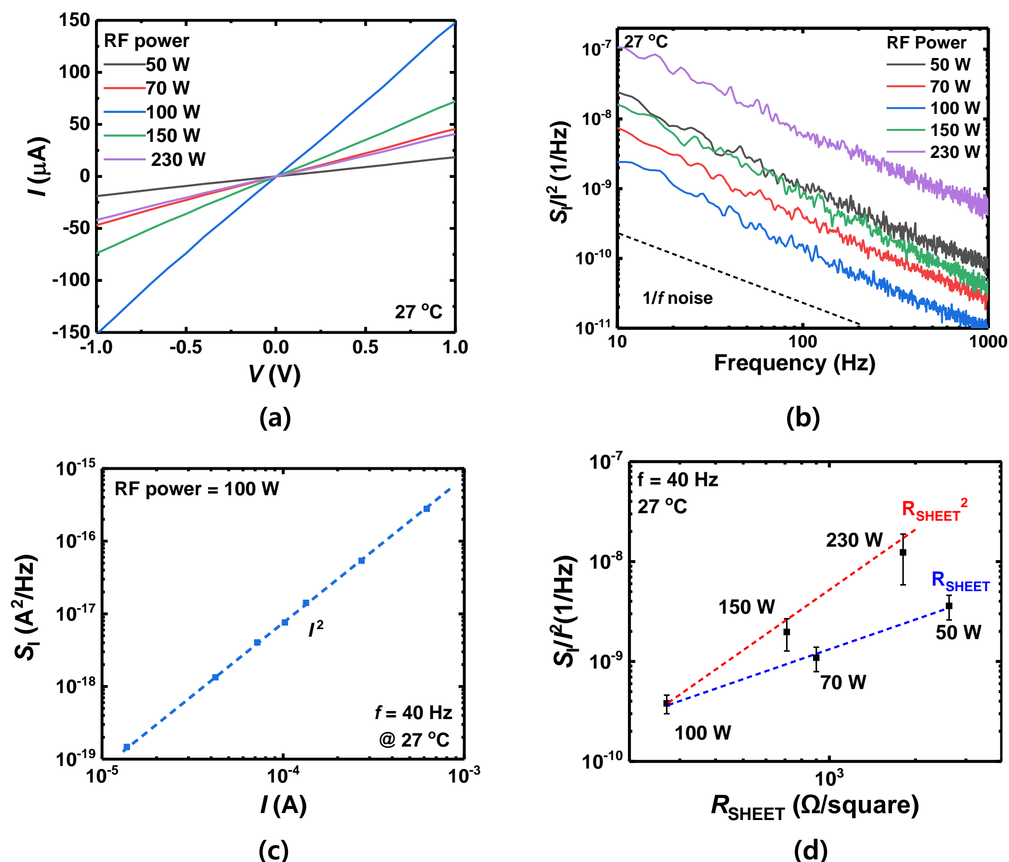

Fig. 5. 2. (a) Current-voltage (I-V) curves of the resistor-type gas sensors fabricated at different RF sputtering powers. (b) S_I/I^2 of the sensors fabricated at different RF sputtering powers. (c) S_I versus I of the sensor having the In_2O_3 with an RF power of 100 W. (d) S_I/I^2 sampled at 40 Hz versus R_{SHEET}.

grain size shrinks and grain boundary scattering rises with decreasing RF power. Contrarily, in the case of resistor-type gas sensors with the sensing layer deposited at high RF power, the LFN properties are mostly governed by the interface between

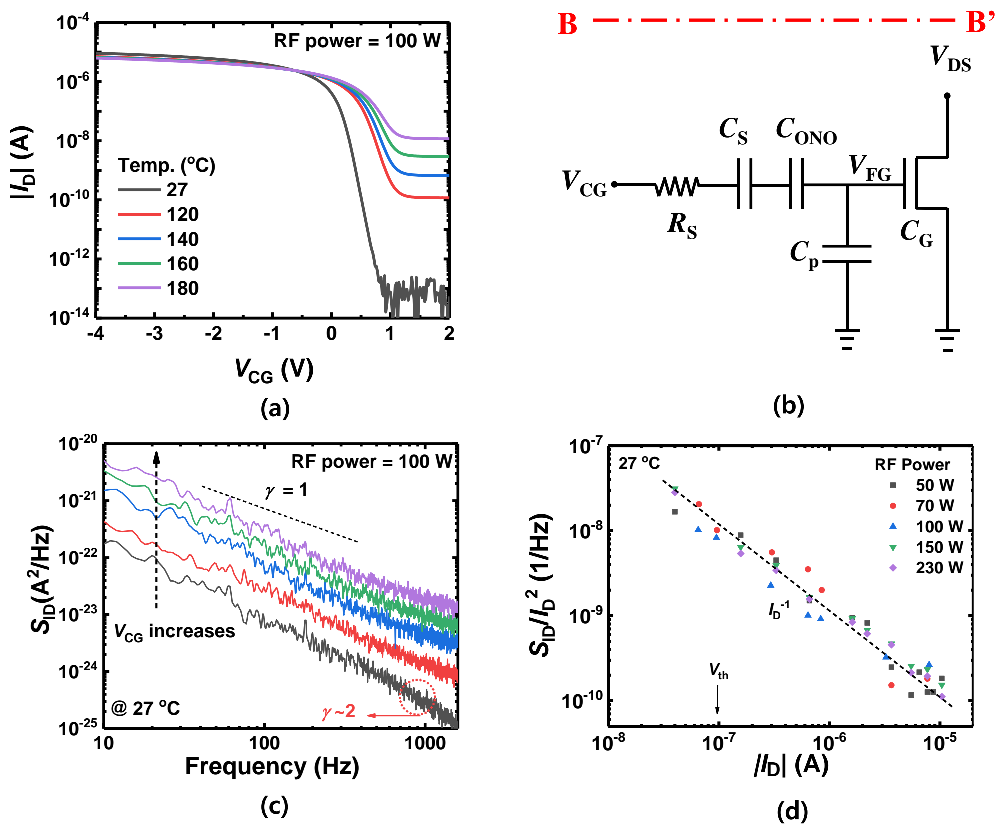

Fig. 5. 3. (a) Drain current-CG voltage curves of FET-type gas sensor measured at various temperatures. (b) Equivalent circuit of the FET-type gas sensor along the dash-dot line B-B'. (c) S_{ID} versus frequency of the sensor deposited at an RF power of 100 W. The V_{CG} is changed while the V_{DS} is fixed. (d) S_{ID}/I_D^2 versus drain current of FET-type gas sensors.

the In_2O_3 and the O/N/O. The damaged interfaces excessively scatter carriers in the In_2O_3 film to contribute to extra CMF, which raises 1/*f* noise [82]. The results indicate that the interface quality that may be damaged during the deposition should thus also be taken into account when fabricating resistor-type gas sensors, even if the majority of previous research concentrates on the surface of the sensing material that interacts with the target gas.

Transfer characteristics of a FET-type gas sensor with sensing material deposited at an RF power of 100 W are shown in Fig. 5.3(a) and evaluated at different temperatures. A FET-type gas sensor equivalent circuit is shown in Fig. 5.3(b). The FET-type gas sensor's LFN power spectra with the sensing layer deposited at an RF power of 100 W at various operating regions are shown in Fig. 5.3(c). At 27 °C, the spectra are measured. A log-log plot of the drain current of FET-type gas sensors' normalized drain current noise recorded at 40 Hz is shown in Fig. 5.3(d). The slope of -1 in the figure, which is evidence that HMF is the cause of the 1/*f* noise in FET-type gas sensors, supports this theory. The inherent noise spectra of FET-type gas sensors have the same LFN properties regardless of the RF

power used to deposit the sensing material. Contrary to resistor-type gas sensors, FET-type gas sensors' LFN properties are unaffected by the circumstances of sensing material deposition. It can be shown that the LFN characteristics of the FET-type gas sensor are dictated by the channel noise of the *p*-type MOSFET since the noise characteristics of the *p*-type MOSFET with FG as its gate electrode are essentially identical to those of the FET-type gas sensors with sensing material.

5.2.3 Comparison of signal-to-noise ratio between resistor- and FET-type gas sensors

In the majority of the research, the current of the sensor is used as a signal, and the response is defined as follows:

$$R(\%) = \left|\frac{I_g - I_o}{I_o}\right| \times 100$$

where I_g and I_o are the currents after and before the interaction of sensors with target gas, respectively.

In Fig. 5.4(a), the upper and lower windows on the *y*-axis show the signal response (ΔI) and root-mean-square current noise amplitude (δI) of resistor-type gas sensors with In_2O_3 deposited at various RF powers. Note that all sensors show

no significant change in conductivity at 180 ºC. ΔI and δI are measured after resistor-type gas sensors are exposed to 50 ppm of H_2S for 100 seconds at 180 ºC.

The signal response (ΔI) and root-mean-square current noise amplitude (δI) of resistor-type gas sensors with In_2O_3 prepared at different RF powers are shown in the upper and lower windows on the y-axis in Fig. 5.4(a). After resistor-type gas sensors are subjected to 50 ppm of H_2S for 100 seconds at 180 ºC, the measurement is conducted. Oxygen is chemisorbed as a charged species in an environment with dry air. The acceptor role of chemisorbed oxygen species traps electrons, reducing In_2O_3's conductivity. H_2S gas molecules interact with adsorbed oxygen and hydroxyl species after coming into contact with In_2O_3 and release the absorbed electron back to the material, increasing the conductivity of the In_2O_3 layer. The extra fluctuation produced by the adsorbed gas may cause the normalized $1/f$ noise

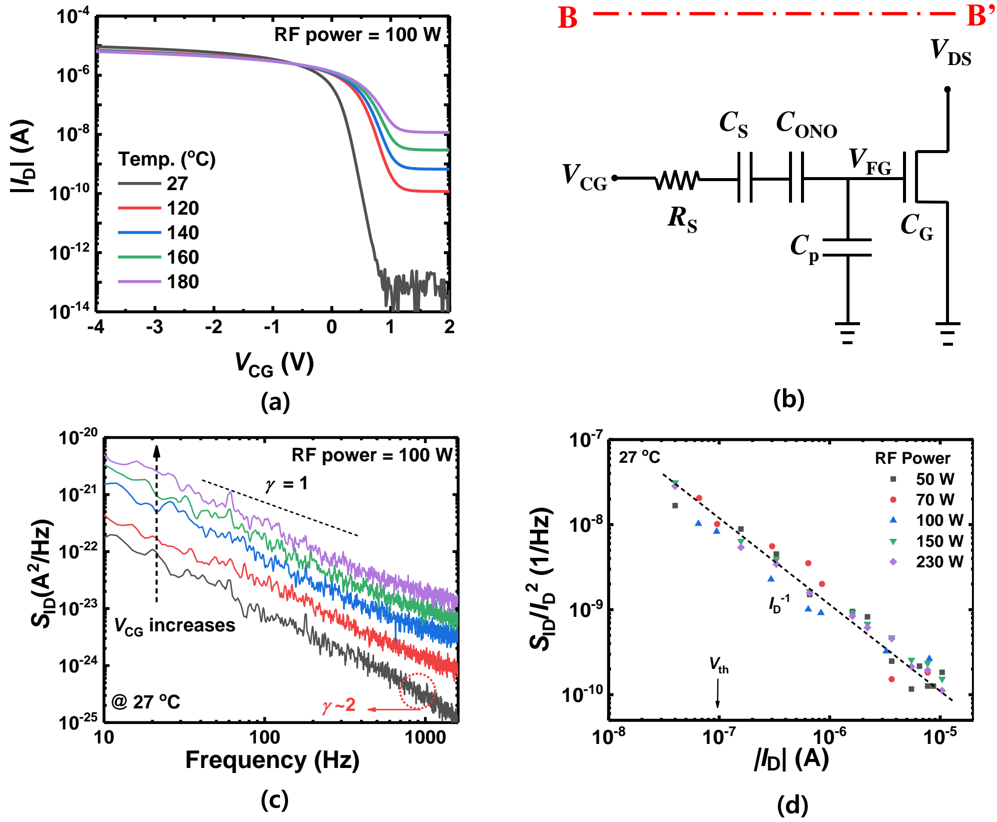

Fig. 5.4. (a) ΔI and δI of resistor-type gas sensors versus I deposited at different RF powers. (b) GANRs of the sensors versus RF power. (c) SNR versus I of the sensors versus RF power. (d) Response versus I of the sensors with different RF powers.

to rise when the resistor-type gas sensors are exposed to the target gas. To assess and compare the LFN features during the gas reaction in both resistor- and FET-type gas sensors, we developed the gas-to-air-noise-ratio (GANR). The ratio of normalized LFN at a fixed frequency before and after the gas reaction is known as

the GANR. The GANRs of resistor-type gas sensors are shown in Fig. 5.4(b). The range of GANRs is 1.35 to 2.24. The SNR and response of resistor-type gas sensors with changes in I are shown in Figs. 5.4(c) and (d), respectively. The SNR of the resistor-type gas sensors has a constant value independent, as illustrated in Fig. 5.4(c). The behavior of noise to RF power behaves in a manner similar to that of the In_2O_3 film's R_{SHEET}. A larger surface-to-volume ratio of the In_2O_3 film is produced by smaller grains, which enhances response. SNR behaves differently from the response when it comes to RF power, however. The bigger δI in the former cancels out the larger response in the latter. It is shown that when RF power increases, noise determines the SNR more so than response.

Transconductance (g_m) curves and signal responses (ΔI_D) of HFGFET-type gas sensors with In_2O_3 deposited at different RF powers are shown in the upper and lower windows on the y-axis. g_ms are measured at 180 °C and ΔI_Ds are measured

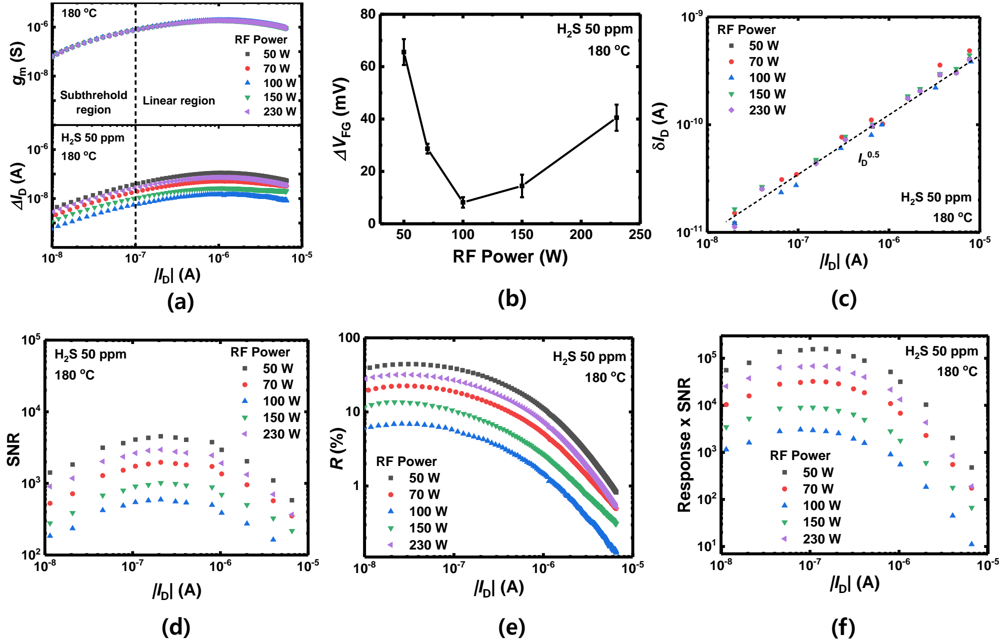

Fig. 5.5. (a) g_m and ΔI_D versus I_D of the FET-type gas sensors with different RF powers. (b) ΔV_{FG} versus RF power. (c) δI_D of the sensors versus I_D. (d) SNR, (e) response, and (f) Response×SNR versus I_D of the sensors with different RF powers, respectively.

after the FET-type gas sensors are exposed to 50 ppm of H_2S at 180 °C for 100 seconds. Regardless of RF power, the g_ms of FET-type gas sensors show similar values. g_m rises when the operating area crosses the threshold from the subthreshold to the linear zone. The g_m reaches saturation and then falls off around the I_D of ~1 μA.

H_2S molecules provide electrons to In_2O_3 during the interaction with the

sensing materials, and this increases the capacitance C_s at the interface between the sensing material and the O/N/O layer by narrowing the depletion area. Then the CG and FG's coupling ratio rises. At the same time, however, H_2S gas molecules that have been positively ionized at the interface between the In_2O_3 and O/N/O layer cause the negative charges to be induced at the FG and O/N/O layer interfaces, causing the positive charge to be induced at the FG and gate interface. As a result, there are fewer holes in the channel, which reduces the I_D magnitude. This change is seen in the MOSFET's g_m, as illustrated in Fig. 5.5(a). The V_x is subject to change in effective charge generated from the gas reaction and can be expressed as

$$\Delta V_X = \frac{\Delta Q_{eff}}{C_{eq}}$$

where ΔQ_{eff} is the total effective charge generated from the reaction between the In_2O_3 and H_2S gas molecules and C_{eq} is the equivalent small-signal capacitance between node V_X and small signal ground.

$$C_{eq} = C_S + \left(\frac{1}{C_{ONO}{}^{-1} + (C_p + C_G)^{-1}}\right).$$

ΔV_X is almost equal to the ΔV_{FG} because the O/N/O capacitance (C_{ONO}) is larger than the capacitance (C_G) between the FG and the channel due to the wide area of

FG. Note that C_p is much smaller than C_G. A positive ΔV_{FG} generated from the ΔQ_{eff} results in a negative ΔI_D in the p-type MOSFET and ΔI_D can be expressed as

$$\Delta I_D = g_m \Delta V_{FG}.$$

ΔI_D and g_m exhibit the same behavior with regard to I_D, as illustrated in Fig. 5.5(a). Figure 5.5(b) depicts the ΔV_{FG} with RF power variations. The relationship between ΔV_{FG} behavior and RF power is dependent on the In_2O_3 film's grain size. The In_2O_3 film has the lowest grain size and the highest surface-to-volume ratio when the sensing material is deposited at a 50 W RF power, resulting in the highest ΔV_{FG}.

The root-mean-square drain current noise amplitude of FET-type gas sensors (δI_D) versus I_D at different RF powers is shown in a log-log plot in Figure 5.5(c). The inherent device noises of FET-type gas sensors are the same independent of the state of the deposition of the sensing material, as illustrated in Fig. 5.5(c). Additionally, the LFN characteristics of the FET-type gas sensors are identical before and after they are exposed to H_2S gas molecules, proving the GANRs of the FET-type gas sensors are 1. As a result, δI_D in the FET-type gas sensors remains constant despite changes in RF power. The SNR of FET-type gas sensors with

respect to I_D is shown as a parameter of RF power in Fig. 5.5(d). With the exception of the fact that the ΔI_D exhibiting the highest SNR (200 nA, which equates to a V_{CG} of V_{th}-0.12 V) is smaller than the I_D exhibiting the highest I_D (1.0 A, which equates to a V_{CG} of V_{th}-0.68 V), SNR behaves in all circumstances in a manner comparable to that of ΔI_D with regard to I_D. This is such that the δI constantly increases with a slope of 0.5 power of I_D, while the ΔI_D saturates and then drops in the linear area. SNR's behavior in relation to RF power mirrors that of the ΔV_{FG}. The sensing material has the highest SNR when it is deposited at 50 W of RF power and the lowest SNR when deposited at 100 W. The FET-type gas sensor's δI_D is independent of the circumstances under which the sensing material is deposited; hence SNR is greatest when the ΔV_{FG} is greatest. According to Fig. 5.5(e), the behavior of response to RF power is the same as that of ΔV_{FG} to RF power. Due to this, when the sensing material is deposited at an RF power of 50 W, as opposed to the resistor-type gas sensor, both response and SNR are at their maximum. In FET-type gas sensors, the operating zones with the maximum response and SNR vary from one another: The subthreshold area has the highest response, but the linear region has

the highest SNR. Response and SNR are multiplied by one another to determine the ideal operating area while concurrently accounting for response and SNR behavior, as illustrated in Fig. 5.5(f). The findings demonstrate that the response's SNR is greatest when the FET-type gas sensor's operating area is set to around 100 nA, an I_D that corresponds to a V_{CG} of V_{th}.

The SNR is used to compare the performance of resistor- and FET-type gas

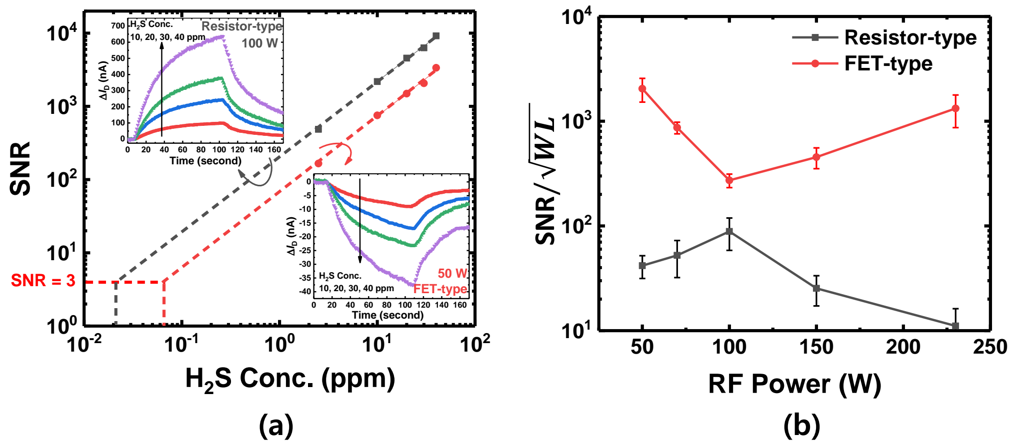

Fig. 5.6. (a) Comparison of SNR between the resistor- and HFGFET-type gas sensors. The upper and lower inserts show the transient gas reaction behavior of resistor- and FET-type gas sensors under the condition where the SNR of each sensor is largest (100 W for resistor-type gas sensors and 50 W for FET-type gas sensors), respectively. (b) SNR per unit channel area (SNR/μm^2) versus RF power of resistor- and FET-type gas sensors.

sensors. Fig. 5.6(a)'s top and lower inserts demonstrate how resistor- and FET-type gas sensors behave during transient gas reactions. The concentration of H_2S gas varies from 10 to 40 ppm. The resistor-type gas sensor's bias voltage is 1 V. The FET-type gas sensor's V_{CG} and V_{DS} are tuned at 0.4 and -0.1 V, respectively, where the response × SNR is greatest. In order to determine the sensors' LOD, the SNR of resistor- and FET-type gas sensors determined at different H_2S gas concentrations is shown in Fig. 5.6(a). The theoretical LOD that corresponds to the SNR value of 3 is determined using the linear extrapolation approach since the gas measuring equipment in our testing apparatus has a limit of 2.5 ppm. Resistor- and FET-type gas sensors have respective LODs of 21 and 67 ppb. The findings show that the sensors can accurately detect extremely low gas concentrations without a strong response, provided they are built and operated with care for noise. Because the SNR of the sensor is related to the square root of the conductive channel area, it is necessary to normalize the SNR to the size of each sensor in order to compare the SNR of resistor- and FET-type gas sensors fairly [73]. The SNR per unit channel area (SNR/ μm^2) of resistor- and FET-type gas sensors is shown in Fig. 5.6(b) as

RF power varies. Compared to resistor-type gas sensors, FET-type gas sensors have an SNR that is at least three times (when In_2O_3 is deposited at an RF power of 100 W) and up to 100 times (deposited at 230 W). This is due to the fact that, although having a poorer response than resistor-type gas sensors, FET-type gas sensors with a sensing layer and current route (MOSFET channel) that are separated produce far less noise. There is no trade-off relationship between response and noise because of the structural uniqueness of FET-type gas sensors. Therefore, the FET-type sensors are chosen as a sensor platform to replace the resistor-type gas sensor if a high SNR is needed.

5.3 Optimization of SNR in HFGFET using transducer and bias condition optimizations

5.3.1 Sensing material characterization

By improving the transducer structure, SNR in HFGFET-type gas sensors can be significantly improved. In this section, an RF magnetron sputtering technique is employed to create a 30 nm-thick *n*-type semiconducting IGZO thin film that is used as a sensing material. Substrate temperature, chamber pressure, an

Ar gas flow rate, and RF power are all set at 27°C, 5 mTorr, 30 sccm, and 50 W, respectively, during the sputtering process.

5.3.2 Comparison of LFN characteristics between the sensors with buried and surface channel FETs

The sensor with an *n*-type FET has an advantage in terms of response because the *n*-type FET has a bigger g_m than the *p*-type FET. The *n*-type FET, however, has significant $1/f$ noise. By altering the channel implantation situation, it is possible to convert the *n*-type FET's surface channel structure to a buried channel structure, which lowers the LFN [34]. The LFN produced by the CNF at the interface may be greatly decreased since the buried channel is built far from the gate oxide-Si substrate interface. In addition to LFN, it has been shown that the electrical properties of FETs with surface channel and buried channel designs vary,

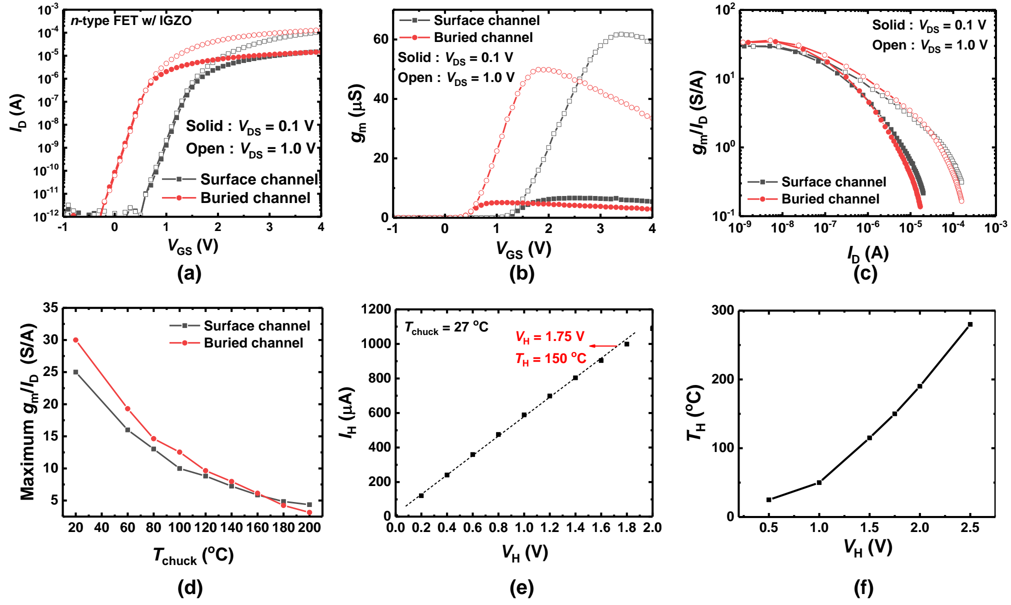

Fig. 5.7. Drain current-CG voltage (I_D-V_{CG}) and (b) g_m of the sensors with buried and surface channel FETs. The V_{DS} is set at 0.1 and 1.0 V. (c) Transconductance efficiency (g_m/I_D) of the sensors with buried and surface channel FETs versus drain current (I_D). (d) Maximum g_m/I_D of the sensors with buried and surface

including g_m, drain-induced barrier lowering, and thermal stability. As a result, a thorough analysis and comparison of the detecting capabilities of FET-type gas sensors with surface and buried channel topologies is necessary.

The transfer characteristics of the sensors with buried and surface channel FETs are shown in Fig. 5.7(a) [83]. The V_{DS} is set at 0.1 and 1.0 V. Due to the excellent gate control capabilities of FET transducers, both sensors exhibit a high

on-off-current-ratio. Due to the implantation of the buried channel, the sensor with the buried channel FET has a lower V_{th} than the one with the surface channel. The sensor with the buried channel FET may thus function with a lower V_{CG} and use less power. In comparison to the sensor with the surface channel FET, the sensor with the buried channel FET exhibits a lower maximum transconductance ($g_{m, max}$) (Fig. 5.7(b)). Because the channel position is constructed distant from the gate oxide-Si substrate interface, the buried channel FET has poorer gate controllability [18]. However, the buried channel FET exhibits a slightly greater g_m/I_D linked with the subthreshold swing (SS), as shown in Fig. 5.7(c). The SSs of the surface and buried channel FETs are 132 and 151 mV/dec, respectively. This is so that the buried channel FET's conductive channel is constructed far from the interface between the silicon substrate's gate oxide and interface states. The maximal g_m/I_D with increasing T_{chuck} is shown in Fig. 5.7(d). The g_m/I_D of the FET transducer has a significant impact on the response of the FET-type gas sensor. The response of the FET-type gas sensor is significantly worsened by the decrease of the g_m/I_D with rising temperature caused by the increased carrier dispersion in the FET channel.

The g_m/I_D value drops more than six times when the T_{chuck} approaches 200 ºC in both buried and surface channel FETs, as illustrated in Fig. 5.7(d). Our research team suggested a localized poly-Si micro-heater to address this issue; it can only increase the temperature of the sensing region while maintaining the FET channel's temperature at ambient temperature. This is due to the fact that the air gap created by the undercut keeps the micro heater's distance from the FET channel, thermally isolating the FET. As a result, it is possible to increase the temperature needed for the gas reaction without harming the g_m/I_D. The current of the micro-heater (I_H) vs V_H as determined by the DC I-V technique is shown in Fig. 5.7(e). The resistance temperature detection (RTD) technique is used to acquire T_H [26].

Fig. 5.8(a) shows the normalized drain current noise spectral density (S_{ID}/I_D^2) of the sensors with buried and surface channel FETs as a function of frequency. Both sensors have $1/f^{\gamma}$ noise behavior with $\gamma \sim 1.0$. The $1/f$ noise behavior in FET devices can be either explained by the CNF or HMF. In the case of CNF, the $1/f$ noise that exceeds the thermal noise in the low-frequency range is generated from the carrier trapping/detrapping at the gate oxide-Si substrate

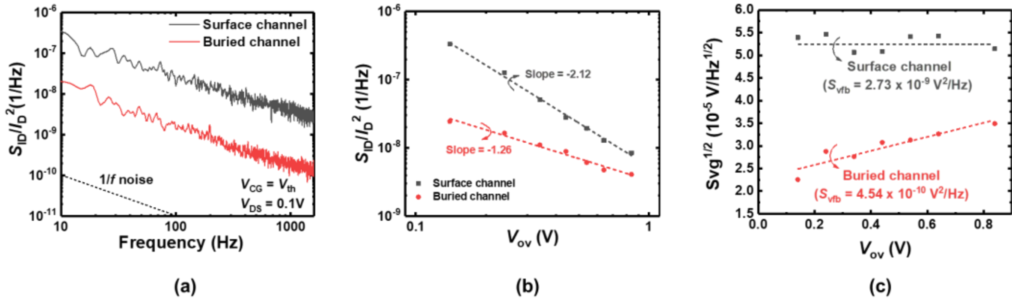

Fig. 5.8. (a) S_{ID}/I_D^2 of the sensors with buried and channel FETs versus frequency. (b) S_{ID}/I_D^2 sampled at 10 Hz versus V_{OV} (c) $\sqrt{S_{vg}}$ versus V_{OV} of the sensors with buried and surface channel FETs.

interface.

The sensors with buried and surface channel FETs are shown with the S_{ID}/I_D^2 of the sensors as a function of frequency in Fig. 5.8(a). Either the CNF or the HMF may be used to describe the 1/*f* noise behavior in FET devices. The slope between -1 and -2 indicates that the 1/*f* noise is generated from the CNF with correlated mobility fluctuation (CMF). According to Ghibaudo et al., CMF is a consequence of the trapped/detrapped carriers in the gate oxide affecting both the carrier mobility and the inversion charge density via the Coulombic interaction. [50]. The log-log plot of the S_{ID}/I_D^2 versus V_{OV}, a parameter of the channel topology, is shown in Fig. 5.8(b). Both sensors have a power-law relationship between the

S_{ID}/I_D^2 sampled at 10 Hz and the V_{OV}, but their slopes are different. While the CNF (slope of -2.13) is primarily where the 1/*f* noise of the surface channel FET originates, the CNF and CMF are where the 1/*f* noise of the buried channel originates (slope of -1.23). The LFN properties are further examined using the CMF model. The CMF model is given as:

$$\frac{S_{ID}}{{I_D}^2} = (1 + \alpha_c \mu_{eff} C_{ox} I_D / g_m)^2 \ (\frac{g_m}{I_D})^2 S_{Vfb} \quad (5)$$

with

$$S_{Vfb} = \frac{q^2 N_t kT\lambda}{WL{C_{ox}}^2 f} \quad (6)$$

where α_c is a Coulomb scattering parameter, μ_{eff} is the effective carrier mobility, S_{Vfb} is the power spectral density of flat band voltage fluctuation, N_t is the volume trap density, and λ is the oxide tunneling attenuation distance. In the linear region, the gate voltage spectral density (S_{vg}) can be expressed as

$$S_{vg} = \frac{S_{ID}}{{g_m}^2} = [1 + \alpha_c \mu_{eff} C_{ox}(V_{gs} - V_{th})]^2 S_{Vfb}. \quad (7)$$

Fig. 5.8(c) exhibits the $\sqrt{S_{vg}}$ as a function of gate overdrive voltage (V_{OV}) of the sensors with buried and surface channel FETs. The sensors with buried and surface channel FETs have the S_{Vfb} of 4.54×10^{-10} and the 2.73×10^{-9} V^2/Hz,

respectively. In the case of the sensor with the surface channel FET, the S_{vg} does not depend on the V_{OV}, which means that the value of α_c is close to zero. This is because the 1/*f* noise of surface channel FET is mostly generated by the CNF. On the other hand, the buried channel FET has an α_c of 1.3×10^{-9} Vs/C, showing the presence of the CMF.

The S_{Vfb} of the sensors with buried channel FETs and surface channel FETs, respectively, is 4.54×10^{-10} and the 2.73×10^{-9} V^2/Hz. The S_{vg} does not rely on the V_{OV} in the case of the sensor with the surface channel FET, indicating that the value of α_c is near zero. This is so because the CNF mostly produces the 1/*f* noise of surface channel FETs. The buried channel FET, on the other hand, has an α_c value of 1.3×10^{-9} Vs/C, indicating the existence of the CMF.

5.3.3 Comparison of NO_2 gas response between the sensors with buried and surface channel FETs

Now, we examine the FET-type gas sensor's NO_2 gas detection capabilities. For a reasonable degree of response and recovery when the IGZO thin film is utilized as a sensing material to detect NO_2, an operating temperature of

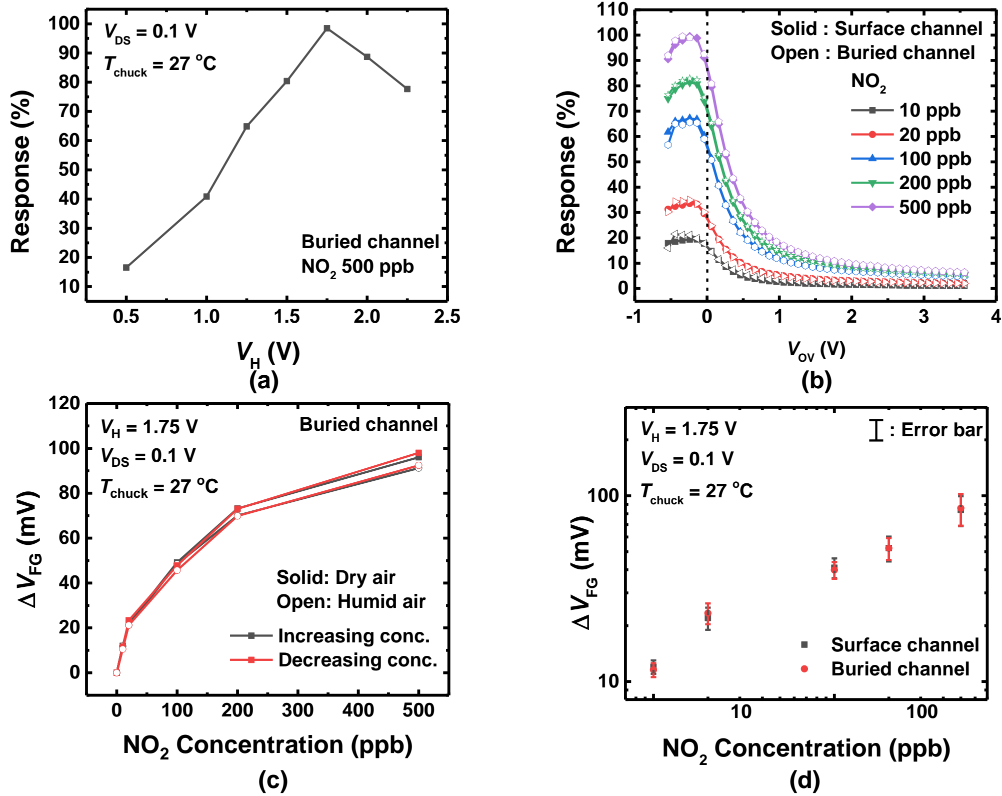

Fig. 5.9. Response versus V_H of the sensor with buried channel FET. The 500 ppb of NO_2 is exposed to the sensor. (b) Response versus V_{OV} measured at different NO_2 gas concentrations. (c) ΔV_{FG} versus NO_2 gas concentration of the sensor with buried channel FET. The solid and open symbols represent the ΔV_{FG} under dry and humid air ambience, respectively. (d) ΔV_{FG} versus NO_2 gas concentration of the sensors measured at four independent samples

above 100 °C is necessary. The response of the sensor with buried channel FET to 500 ppb of NO_2 versus V_H is shown in Fig. 5.9(a). When the V_H is set to 1.75 V, the sensor response is the largest. The response of the sensors with buried and surface

channel FETs as a parameter of NO_2 gas concentration is shown in Fig. 5.9(b). Due to its greater g_m/I_D, the response of the sensor with buried channel FET is slightly bigger than that of surface channel FET. The sensor with buried channel FET's ΔV_{FG} versus NO_2 concentration is shown in Fig. 5.9(c). The sensors exhibit hysteresis-free behaviors and no memory effect. The log-log plot of the ΔV_{FG} versus NO_2 concentration as a parameter of the channel topology for four different samples is shown in Fig. 5.9(d).

5.3.4 Comparison of signal-to-noise ratio gas response between the sensors with buried and surface channel FETs

The SNR of the sensors with the buried and surface channel FETs is calculated by changing V_{DS}s and V_{CG}s. The linear mode (V_{DS} = 0.1 V) and saturation

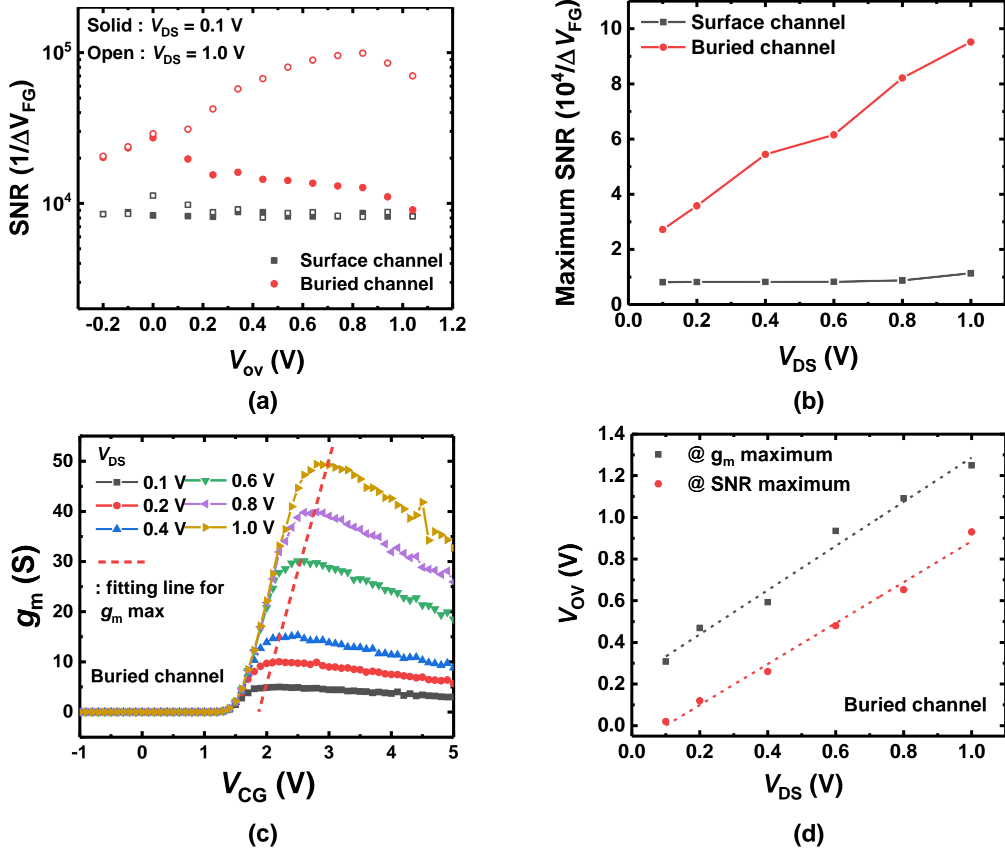

Fig. 5.10. SNR per unit ΔV_{FG} versus V_{OV} of the sensors calculated at V_{DS} of 0.1 and 1.0 V. (b) Maximum SNR versus V_{DS} of the sensors with different channel structures. (c) g_m versus V_{CG} measured at different V_{DS}s. (d) Optimal V_{OV} where the largest g_m and SNR are observed versus V_{DS}.

mode (V_{DS} = 1.0 V) are represented by two V_{DS} values. Fig. 5.10(a) displays the SNR per unit ΔV_{FG} of the sensors using buried and surface channel FETs. At both V_{DS}s of 0.1 and 1.0 V, the surface channel sensor exhibits no influence of SNR on the operating region. This is because S_{Vfb} is a weak function of V_{DS} when the CNF

generates the 1/*f* noise of the surface channel FET [27].

Additionally, S_{ID}/I_D^2 behavior is proportional to $(g_m/I_D)^2$. As a result, SNR exhibits no region dependency, and both ΔI_D and δI_D are proportional to g_m. On the other hand, since the g_m grows more abruptly with rising V_{CG} than the I_D, the behavior of SNR in buried channel FETs follows that of g_m. As a result, the V_{CG}, which is almost the same as the location where the g_m is the biggest, is where the SNR of the sensor with buried channel FET is at its highest. Because the I_D likewise rises with increasing V_{CG}, there is little difference between V_{CG}s when the g_m and SNR are the maxima. The buried channel has the largest SNR when the FET operates at V_{OV} = 0 V for V_{DS} = 0.1 V. Also, as the g_m is proportional to V_{DS} in the linear region, the signal can be increased by increasing V_{DS}. Additionally, because the g_m in the linear region is proportional to V_{DS}, an increase of V_{DS} boosts the signal. If the V_{DS} is greater than kT/q, the 1/*f* noise produced mostly by the HMF is independent of V_{DS} [28]. Therefore, raising the V_{DS} will result in further improvement of the SNR. The highest SNR versus V_{DS} is shown as a channel structure parameter in Fig. 5.10(b). The sensor with the surface channel has no

dependency on the V_{DS}, but the SNR of the sensor with the buried channel FET rises with increasing V_{DS}. The g_m curves of the sensor with buried channel FET as a parameter of V_{DS} are shown in Fig. 5.10(c). The V_{DS} and V_{CG} in the sensor can be controlled using a buried channel FET to enhance SNR, as shown in Fig. 5.11(d).

The log-log plot of the SNR of the sensors with buried and surface channel FETs against NO_2 gas concentration is shown in Fig. 5.11(a). The sensor with the buried channel FET has the larger SNR across all gas concentrations. The LOD of the sensor is determined from the power-law dependency between SNR and NO_2

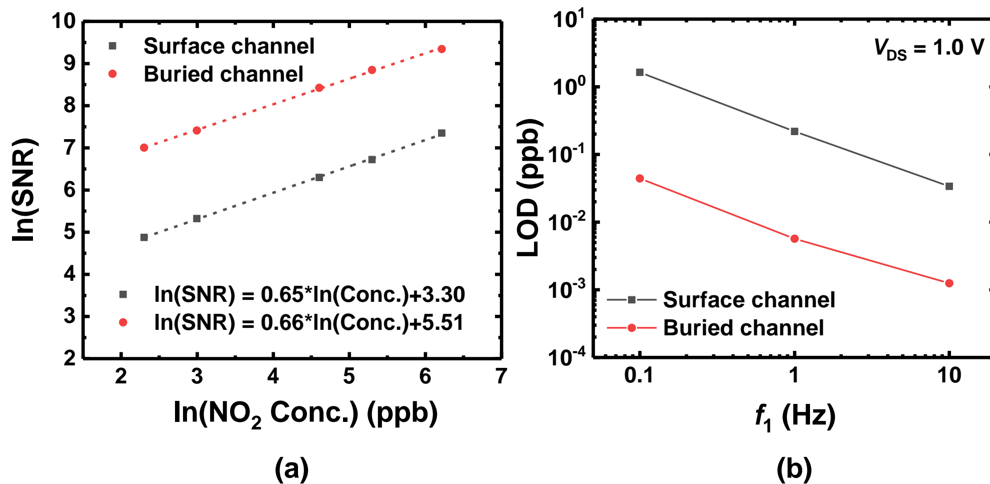

Fig. 5.11. SNR versus NO_2 gas concentration of the sensors. (b) Evaluated LOD versus f_1 of the sensors.

gas concentration. The LODs of the sensor with surface and buried channel FETs are 0.03 ppb and 1.25 ppt, respectively, in the frequency range of 10 Hz to 1600 Hz. The LOD is obtained for the sensor with the surface channel FET at V_{OV} = 0 V and V_{DS} = 0.1 V and for the sensor with the buried channel FET at V_{OV} = 0.83 V and V_{DS} = 1.0 V. It is also investigated how much the LOD of the buried channel FET depends on the BW. The LOD obtained at different measurement bandwidths is shown as a channel structure parameter in Fig. 5.11(b). At a constant f_2 of 1600 Hz, the f_1 fluctuates between 0.1 and 10 Hz. When the f_1 is reduced from 10 to 0.1 Hz in the instance of the sensor with the buried channel FET, the LOD of the sensor rises from 1.25 to 44.2 ppt.

We demonstrated that in the fabrication of FET-type gas sensors, not only the response but also the noise should be taken into account. The LFN properties should be taken into account while designing and fabricating the transducer. The significance of noise reduction has long been acknowledged in biosensors or pressure sensors. Accordingly, the improvement of the LFN properties of the transducer has received significant attention. However, studies on gas sensors have

not paid enough attention to optimizing the LFN properties in the FET transducer. To close this gap, we examined how the FET channel structure affects the LFN properties. We also examined how channel structure and operating bias parameters could be optimized to increase the SNR and LOD of FET-type gas sensors. The SNR of the buried channel sensor is around ten times greater, even if the response of the sensors with buried and surface channel FETs is not noticeably different. Because there is less noise generated from the Si/SiO_2 interface in the buried channel FET, it has a higher SNR than the surface channel FET. This study offers crucial instructions for fabricating low-noise sensors and optimizing the operation of HFGFET-type gas sensors.

Chapter 6

Conclusions

In this dissertation, the LFN characteristics of the HFGFET-type gas sensors are demonstrated. Effects of different sensing materials (In_2O_3 and WO_3) and sensor platforms (resistor- and HFGFET-type gas sensors) on LFN characteristics of sensors are investigated, which allows revealing the noise-generating mechanisms in the HFGFET-type gas sensors. There are two main noise-generating mechanisms in the HFGFET-type gas sensors: charge fluctuation generated 1) from the carrier scattering at the FET transducer used as a sensor platform and 2) from the sensing material. When the magnitude of resistance of sensing material is small as in the case of In_2O_3, the LFN characteristics of the HFGFET-type gas sensors are determined by the charge fluctuation at the channel of the FET transducer. In this case, depending on the structure of the FET transducer (surface or buried channel), the $1/f$ noise of the sensor differs; CNF or HMF. When the LFN of the HFGFET-type gas sensor is determined by the FET channel, the magnitude of $1/f$ noise of the

HFGFET-type gas sensor is much smaller than that of the resistor-type gas sensors. Thus, the larger SNR and lower LoD can be achieved by adopting the HFGFET-type gas sensors as a sensor platform. In the case where the resistance of the sensing material is large as WO_3, the LFN of the HFGFET-type gas sensors is determined by the charge fluctuation at the sensing material. The charge fluctuation is generated from the carrier exchange between the sensing material and gas molecules. Accordingly, the shot noise is generated, and this noise is transferred to the voltage fluctuation by the RC network inside the sensing material. Thus, the PSD of the sensor has the form of the Lorentzian-like noise whose f_c is determined by the RC network. In this case, the LFN characteristics of the HFGFET-type gas sensors can be utilized to realize selective detection. LFN spectroscopy to selectively detect the target gas is presented.

As aforementioned, the majority of previous studies on gas sensors focused on response, selectivity, and sensitivity. However, as this dissertation demonstrated, the LFN of sensors plays a significant role in various performances of the sensors. LFN in gas sensors may need to be reduced to accomplish large SNR and low LoD,

or to be utilized for selectivity, depending on the application. Thus, the LFN should be carefully regulated depending on the application of the gas sensor, and it's crucial to have the right expertise to make this engineering feasible. This dissertation offers a solid platform on which this can be achieved.

Bibliography

[1] D. Wang *et al.*, “Ethylene chlorotrifluoroethylene/hydrogel-based liquid-solid triboelectric nanogenerator driven self-powered MXene-based sensor system for marine environmental monitoring,” *Nano Energy*, vol. 100, Sep. 2022, doi: 10.1016/j.nanoen.2022.107509.

[2] H. Tai, S. Wang, Z. Duan, and Y. Jiang, “Evolution of breath analysis based on humidity and gas sensors: Potential and challenges,” *Sensors and Actuators, B: Chemical*, vol. 318. Elsevier B.V., Sep. 01, 2020. doi: 10.1016/j.snb.2020.128104.

[3] H. Wan, Y. Gan, J. Sun, T. Liang, S. Zhou, and P. Wang, “High sensitive reduced graphene oxide-based room temperature ionic liquid electrochemical gas sensor with carbon-gold nanocomposites amplification,” *Sens Actuators B Chem*, vol. 299, Nov. 2019, doi: 10.1016/j.snb.2019.126952.

[4] S. Dhall, B. R. Mehta, A. K. Tyagi, and K. Sood, “A review on environmental gas sensors: Materials and technologies,” *Sensors International*, vol. 2. KeAi Communications Co., Jan. 01, 2021. doi: 10.1016/j.sintl.2021.100116.

[5] D. Punetha and S. K. Pandey, “Sensitivity Enhancement of Ammonia Gas Sensor Based on Hydrothermally Synthesized rGO/WO3 Nanocomposites,” *IEEE Sens J*, vol. 20, no. 4, pp. 1738–1745, Feb. 2020, doi: 10.1109/JSEN.2019.2950781.

[6] A. K. Maw, P. Somboon, W. Srituravanich, and A. Teeramongkonrasmee, “A Hybrid E-nose System based on Metal Oxide Semiconductor Gas Sensors and Compact Colorimetric Sensors,” in *2021 IEEE International Conference on Automatic Control and Intelligent Systems, I2CACIS 2021 - Proceedings*, Jun. 2021, pp. 352–357. doi: 10.1109/I2CACIS52118.2021.9495905.

[7] F. Tian, A. Jiang, T. Yang, J. Qian, R. Liu, and M. Jiang, “Application of Fractal Geometry in Gas Sensor: A Review,” *IEEE Sens J*, vol. 21, no. 13, pp. 14587–14600, Jul. 2021, doi: 10.1109/JSEN.2021.3072621.

[8] M. Vafaei, A. Amini, and A. Siadatan, “Breakthrough in CO2 Measurement with a Chamberless NDIR Optical Gas Sensor,” *IEEE Trans Instrum Meas*, vol. 69, no. 5, pp. 2258–2268, May 2020, doi: 10.1109/TIM.2019.2920702.

[9] T. Xiao, J. Huang, D. Wang, T. Meng, and X. Yang, “Au and Au-Based nanomaterials: Synthesis and recent progress in electrochemical sensor applications,” *Talanta*, vol. 206.

Elsevier B.V., Jan. 01, 2020. doi: 10.1016/j.talanta.2019.120210.

[10] L. Zhang, K. Khan, J. Zou, H. Zhang, and Y. Li, "Recent Advances in Emerging 2D Material-Based Gas Sensors: Potential in Disease Diagnosis," *Advanced Materials Interfaces*, vol. 6, no. 22. Wiley-VCH Verlag, Nov. 01, 2019. doi: 10.1002/admi.201901329.

[11] S. Yuvaraja, V. N. Bhyranalyar, S. A. Bhat, S. G. Surya, C. V. Yelamaggad, and K. N. Salama, "A highly selective electron affinity facilitated H2S sensor: The marriage of tris(keto-hydrazone) and an organic field-effect transistor," *Mater Horiz*, vol. 8, no. 2, pp. 525–537, Feb. 2021, doi: 10.1039/d0mh01420f.

[12] S. Absalan, S. Nasresfahani, and M. H. Sheikhi, "High-performance carbon monoxide gas sensor based on palladium/tin oxide/porous graphitic carbon nitride nanocomposite," *J Alloys Compd*, vol. 795, pp. 79–90, Jul. 2019, doi: 10.1016/j.jallcom.2019.04.187.

[13] Y. Tu *et al.*, "Ammonia Gas Sensor Response of a Vertical Zinc Oxide Nanorod-Gold Junction Diode at Room Temperature," *ACS Sens*, vol. 5, no. 11, pp. 3568–3575, Nov. 2020, doi: 10.1021/acssensors.0c01769.

[14] N. Liu *et al.*, "Tunable NH4F-Assisted Synthesis of 3D Porous In2O3Microcubes for Outstanding NO2Gas-Sensing Performance: Fast Equilibrium at High Temperature and Resistant to Humidity at Room Temperature," *ACS Appl Mater Interfaces*, vol. 13, no. 12, pp. 14355–14364, Mar. 2021, doi: 10.1021/acsami.0c22987.

[15] M. Punginsang *et al.*, "Selective H2S gas sensors based on ohmic hetero-interface of Au-functionalized WO3 nanowires," *Appl Surf Sci*, vol. 571, Jan. 2022, doi: 10.1016/j.apsusc.2021.151262.

[16] A. Nathan and S. Jeon, "Oxide electronics: Translating materials science from lab-to-fab," *MRS Bulletin*, vol. 46, no. 11. Springer Nature, pp. 1028–1036, Nov. 01, 2021. doi: 10.1557/s43577-021-00257-3.

[17] B. Kwon *et al.*, "Ultrasensitive N-Channel Graphene Gas Sensors by Nondestructive Molecular Doping," *ACS Nano*, vol. 16, no. 2, pp. 2176–2187, Feb. 2022, doi: 10.1021/acsnano.1c08186.

[18] P. Goswami and G. Gupta, "Recent progress of flexible NO2 and NH3 gas sensors based on transition metal dichalcogenides for room temperature sensing," *Materials Today Chemistry*, vol. 23. Elsevier Ltd, Mar. 01, 2022. doi: 10.1016/j.mtchem.2021.100726.

[19] Y. Xu *et al.*, "End Group Modification for Black Phosphorus: Simultaneous Improvement

of Chemical Stability and Gas Sensing Performance,” *ACS Appl Mater Interfaces*, vol. 13, no. 42, pp. 50270–50280, Oct. 2021, doi: 10.1021/acsami.1c16776.

[20] R. Bhardwaj and A. Hazra, “MXene-based gas sensors,” *Journal of Materials Chemistry C*, vol. 9, no. 44. Royal Society of Chemistry, pp. 15735–15754, Nov. 28, 2021. doi: 10.1039/d1tc04085e.

[21] G. Drera *et al.*, “Exploring the performance of a functionalized CNT-based sensor array for breathomics through clustering and classification algorithms: From gas sensing of selective biomarkers to discrimination of chronic obstructive pulmonary disease,” *RSC Adv*, vol. 11, no. 48, pp. 30270–30282, Sep. 2021, doi: 10.1039/d1ra03337a.

[22] Z. Zhu *et al.*, “Flexible fiber-shaped hydrogen gas sensor via coupling palladium with conductive polymer gel fiber,” *J Hazard Mater*, vol. 411, Jun. 2021, doi: 10.1016/j.jhazmat.2020.125008.

[23] A. K. Singh, N. K. Chowdhury, S. C. Roy, and B. Bhowmik, “Review of Thin Film Transistor Gas Sensors: Comparison with Resistive and Capacitive Sensors,” *Journal of Electronic Materials*, vol. 51, no. 5. Springer, pp. 1974–2003, May 01, 2022. doi: 10.1007/s11664-022-09485-y.

[24] G. Jung *et al.*, “Design optimization of FET-type gas sensor considering device characteristics, sensitivity, power, noise, and SNR,” *Sens Actuators B Chem*, vol. 369, Oct. 2022, doi: 10.1016/j.snb.2022.132257.

[25] I. Eisele, T. Doll, and M. Burgmair, “Low power gas detection with FET sensors.” [Online]. Available: http://www.unibw-muenchen.de/campus/ET9.

[26] W. Shin *et al.*, “Synergistic improvement of sensing performance in ferroelectric transistor gas sensors using remnant polarization,” *Mater Horiz*, vol. 9, no. 6, pp. 1623–1630, Apr. 2022, doi: 10.1039/d2mh00340f.

[27] G. Jung *et al.*, “A low-power embedded poly-Si micro-heater for gas sensor platform based on a FET transducer and its application for NO2 sensing,” *Sens Actuators B Chem*, vol. 334, May 2021, doi: 10.1016/j.snb.2021.129642.

[28] R.-H. Koo *et al.*, “Power Efficient Read Bias Scheme of the Synaptic Devices for Neuromorphic Applications.” [Online]. Available: www.dbpia.co.kr

[29] W. Shin *et al.*, “Comprehensive and accurate analysis of the working principle in ferroelectric tunnel junctions using low-frequency noise spectroscopy,” *Nanoscale*, vol. 14,

no. 6, pp. 2177–2185, Feb. 2022, doi: 10.1039/d1nr06525d.

[30] S. Hong *et al.*, “FET-type gas sensors: A review,” *Sensors and Actuators, B: Chemical*, vol. 330. Elsevier B.V., Mar. 01, 2021. doi: 10.1016/j.snb.2020.129240.

[31] Y. Jeong *et al.*, “Highly stable Si MOSFET-type humidity sensor with ink-jet printed graphene quantum dots sensing layer,” *Sens Actuators B Chem*, vol. 343, Sep. 2021, doi: 10.1016/j.snb.2021.130134.

[32] S. Hong *et al.*, “Improved CO gas detection of Si MOSFET gas sensor with catalytic Pt decoration and pre-bias effect,” *Sens Actuators B Chem*, vol. 300, Dec. 2019, doi: 10.1016/j.snb.2019.127040.

[33] D. Kwon *et al.*, “Efficient fusion of spiking neural networks and FET-type gas sensors for a fast and reliable artificial olfactory system,” *Sens Actuators B Chem*, vol. 345, Oct. 2021, doi: 10.1016/j.snb.2021.130419.

[34] W. Shin *et al.*, “Efficient improvement of sensing performance using charge storage engineering in low noise FET-type gas sensors,” in *Technical Digest - International Electron Devices Meeting, IEDM*, Dec. 2020, vol. 2020-December, pp. 35.3.1-35.3.4. doi: 10.1109/IEDM13553.2020.9371920.

[35] D. Kwon *et al.*, “Low-power and reliable gas sensing system based on recurrent neural networks,” *Sens Actuators B Chem*, vol. 340, Aug. 2021, doi: 10.1016/j.snb.2020.129258.

[36] W. Shin *et al.*, “Effects of IGZO film thickness on H2S gas sensing performance: Response, excessive recovery, low-frequency noise, and signal-to-noise ratio,” *Sens Actuators B Chem*, vol. 344, Oct. 2021, doi: 10.1016/j.snb.2021.130148.

[37] G. Jung *et al.*, “Comparison of the characteristics of semiconductor gas sensors with different transducers fabricated on the same substrate,” *Sens Actuators B Chem*, vol. 335, May 2021, doi: 10.1016/j.snb.2021.129661.

[38] M. Inaba *et al.*, “Effect of mixing ratio on NO2 gas sensor response with SnO2-decorated carbon nanotube channels fabricated by one-step dielectrophoretic assembly,” *Sens Actuators B Chem*, vol. 344, Oct. 2021, doi: 10.1016/j.snb.2021.130257.

[39] J. Qin *et al.*, “Carbon nanodot-based humidity sensor for self-powered respiratory monitoring,” *Nano Energy*, vol. 101, p. 107549, Oct. 2022, doi: 10.1016/j.nanoen.2022.107549.

[40] A. Kumar, Y. Zhao, M. M. Mohammadi, J. Liu, T. Thundat, and M. T. Swihart, “Palladium

Nanosheet-Based Dual Gas Sensors for Sensitive Room-Temperature Hydrogen and Carbon Monoxide Detection," *ACS Sens*, vol. 7, no. 1, pp. 225–234, Jan. 2022, doi: 10.1021/acssensors.1c02015.

[41] D. N. Son *et al.*, "A novel design and fabrication of self-heated In2O3 nanowire gas sensor on glass for ethanol detection," *Sens Actuators A Phys*, vol. 345, Oct. 2022, doi: 10.1016/j.sna.2022.113769.

[42] Q. Q. Chen *et al.*, "Au@ZIF-8 Core-Shell Nanoparticles as a SERS Substrate for Volatile Organic Compound Gas Detection," *Anal Chem*, vol. 93, no. 19, pp. 7188–7195, May 2021, doi: 10.1021/acs.analchem.0c05432.

[43] H. Fu *et al.*, "Gas-sensing performance of In2O3@MoO3 hollow core-shell nanospheres prepared by a two-step hydrothermal method," *Sens Actuators B Chem*, vol. 352, Feb. 2022, doi: 10.1016/j.snb.2021.131007.

[44] K. B. Kim, S. Y. Jeong, T. H. Kim, Y. C. Kang, and J. H. Lee, "Methylbenzene sensors using Ti-doped NiO multiroom spheres: Versatile tunability on selectivity, response, sensitivity, and detection limit," *Sens Actuators B Chem*, vol. 308, Apr. 2020, doi: 10.1016/j.snb.2020.127730.

[45] S. Zaunseder, A. Vehkaoja, V. Fleischhauer, and C. Hoog Antink, "Signal-to-noise ratio is more important than sampling rate in beat-to-beat interval estimation from optical sensors," *Biomed Signal Process Control*, vol. 74, Apr. 2022, doi: 10.1016/j.bspc.2022.103538.

[46] Y. K. Moon, S. Y. Jeong, Y. M. Jo, Y. K. Jo, Y. C. Kang, and J. H. Lee, "Highly Selective Detection of Benzene and Discrimination of Volatile Aromatic Compounds Using Oxide Chemiresistors with Tunable Rh-TiO2 Catalytic Overlayers," *Advanced Science*, vol. 8, no. 6, Mar. 2021, doi: 10.1002/advs.202004078.

[47] W. Shin *et al.*, "Unveiling Resistance Switching Mechanisms in Undoped HfO_x Ferroelectric Tunnel Junction Using Low-Frequency Noise Spectroscopy," *IEEE Electron Device Letters*, pp. 1–1, 2022, doi: 10.1109/LED.2022.3231809.

[48] R. H. Koo *et al.*, "Effect of Carrier Transport Process on Tunneling Electroresistance in Ferroelectric Tunnel Junction," *IEEE Electron Device Letters*, 2022, doi: 10.1109/LED.2022.3223340.

[49] W. Shin *et al.*, "Effect of charge storage engineering on the NO2gas sensing properties of a WO3FET-type gas sensor with a horizontal floating-gate," *Nanoscale*, vol. 13, no. 19, pp.

9009–9017, May 2021, doi: 10.1039/d1nr00513h.

[50] W. Shin *et al.*, "Improved signal-to-noise-ratio of FET-type gas sensors using body bias control and embedded micro-heater," *Sens Actuators B Chem*, vol. 329, Feb. 2021, doi: 10.1016/j.snb.2020.129166.

[51] G. Jung *et al.*, "Optimal Bias Conditions for FET-type Gas Sensors to Minimize Current Fluctuations," in *International Symposium on Olfaction and Electronic Nose, ISOEN 2022 - Proceedings*, 2022. doi: 10.1109/ISOEN54820.2022.9789643.

[52] G. Jung *et al.*, "SO2 gas sensing characteristics of FET- and resistor-type gas sensors having WO3 as sensing material," *Solid State Electron*, vol. 165, Mar. 2020, doi: 10.1016/j.sse.2019.107747.

[53] W. Shin *et al.*, "Effects of High-Pressure Annealing on the Low-Frequency Noise Characteristics in Ferroelectric FET," *IEEE Electron Device Letters*, vol. 43, no. 1, pp. 13–16, Jan. 2022, doi: 10.1109/LED.2021.3127175.

[54] W. Shin *et al.*, "Effects of Channel Length Scaling on the Signal-To-Noise Ratio in FET-Type Gas Sensor with Horizontal Floating-Gate," *IEEE Electron Device Letters*, vol. 43, no. 3, pp. 442–445, Mar. 2022, doi: 10.1109/LED.2022.3145374.

[55] W. Shin *et al.*, "Fully integrated FET-type gas sensor with optimized signal-to-noise ratio for H2S gas detection," *Sens Actuators B Chem*, vol. 367, Sep. 2022, doi: 10.1016/j.snb.2022.132052.

[56] W. Shin *et al.*, "Optimization of post-deposition annealing temperature for improved signal-To-noise ratio in In2O3gas sensor," *Semicond Sci Technol*, vol. 36, no. 7, Jul. 2021, doi: 10.1088/1361-6641/abf906.

[57] W. Shin *et al.*, "Investigation of Low-Frequency Noise Characteristics of Ferroelectric Tunnel Junction: From Conduction Mechanism and Scaling Perspectives," *IEEE Electron Device Letters*, vol. 43, no. 6, pp. 958–961, Jun. 2022, doi: 10.1109/LED.2022.3168797.

[58] W. Shin *et al.*, "Variability analysis of ferroelectric FETs in program operation using low-frequency noise spectroscopy," *Appl Phys Lett*, vol. 121, no. 16, Oct. 2022, doi: 10.1063/5.0111309.

[59] W. Shin *et al.*, "Low frequency noise characteristics of resistor- and Si MOSFET-type gas sensors fabricated on the same Si wafer with In2O3 sensing layer," *Sens Actuators B Chem*, vol. 318, Sep. 2020, doi: 10.1016/j.snb.2020.128087.

[60] W. Shin *et al.*, “Highly Efficient Self-Curing Method in MOSFET Using Parasitic Bipolar Junction Transistor,” *IEEE Electron Device Letters*, vol. 43, no. 7, pp. 1001–1004, Jul. 2022, doi: 10.1109/LED.2022.3176238.

[61] S. Hong *et al.*, “Macroscopic analysis and design of Si HFGFET gas sensor for sensitive gas detection,” *Solid State Electron*, vol. 200, Feb. 2023, doi: 10.1016/j.sse.2022.108545.

[62] J. Park *et al.*, “H2S gas sensing properties in polysilicon control-gate FET-type gas sensor,” *Solid State Electron*, vol. 200, Feb. 2023, doi: 10.1016/j.sse.2022.108543.

[63] Y. Jeong *et al.*, “Effects of oxygen gas in the sputtering process of the WO3 sensing layer on NO2 sensing characteristics of the FET-type gas sensor,” *Solid State Electron*, vol. 200, Feb. 2023, doi: 10.1016/j.sse.2022.108563.

[64] G. Jung *et al.*, “Highly Selective and Low-Power Carbon Monoxide Gas Sensor Based on the Chain Reaction of Oxygen and Carbon Monoxide to WO3,” *ACS Appl Mater Interfaces*, vol. 14, no. 15, pp. 17950–17958, Apr. 2022, doi: 10.1021/acsami.1c25221.

[65] J. Wang, H. Shen, Y. Xia, and S. Komarneni, “Light-activated room-temperature gas sensors based on metal oxide nanostructures: A review on recent advances,” *Ceramics International*, vol. 47, no. 6. Elsevier Ltd, pp. 7353–7368, Mar. 15, 2021. doi: 10.1016/j.ceramint.2020.11.187.

[66] W. Zheng, X. Zhao, and W. Fu, “Review of Vertical Graphene and its Applications,” *ACS Applied Materials and Interfaces*, vol. 13, no. 8. American Chemical Society, pp. 9561–9579, Mar. 03, 2021. doi: 10.1021/acsami.0c19188.

[67] X. Chen, C. Liu, and S. Mao, “Environmental Analysis with 2D Transition-Metal Dichalcogenide-Based Field-Effect Transistors,” *Nano-Micro Letters*, vol. 12, no. 1. Springer, Apr. 01, 2020. doi: 10.1007/s40820-020-00438-w.

[68] W. Shin *et al.*, “Low frequency noise characteristics of resistor- and Si MOSFET-type gas sensors fabricated on the same Si wafer with In2O3 sensing layer,” *Sens Actuators B Chem*, vol. 318, Sep. 2020, doi: 10.1016/j.snb.2020.128087.

[69] M. Al-Hashem, S. Akbar, and P. Morris, “Role of Oxygen Vacancies in Nanostructured Metal-Oxide Gas Sensors: A Review,” *Sensors and Actuators, B: Chemical*, vol. 301. Elsevier B.V., Dec. 12, 2019. doi: 10.1016/j.snb.2019.126845.

[70] W. Shin, K. K. Min, D. Kwon, B.-G. Park, and J.-H. Lee, “Effects of Bias Condition on Low-Frequency Noise Characteristics in Ferroelectric-Based Memories.” [Online].

Available: www.dbpia.co.kr

[71] W. Shin, S. Hong, Y. Jeong, G. Jung, B. G. Park, and J. H. Lee, “Effects of Postdeposition Annealing Ambience on NO2Gas Sensing Performance in Si-Based FET-Type Gas Sensor,” *IEEE Trans Electron Devices*, vol. 69, no. 5, pp. 2604–2610, May 2022, doi: 10.1109/TED.2022.3161246.

[72] D. Kim *et al.*, “Effects of Electrode Structure on H2S Sensing and Low-Frequency Noise Characteristics in In2O3-Based Resistor-Type Gas Sensors,” *IEEE Sens J*, vol. 22, no. 7, pp. 6311–6320, Apr. 2022, doi: 10.1109/JSEN.2022.3154417.

[73] W. Shin, D. Kwon, J. H. Bae, S. Lim, B. G. Park, and J. H. Lee, “Impacts of Program/Erase Cycling on the Low-Frequency Noise Characteristics of Reconfigurable Gated Schottky Diodes,” *IEEE Electron Device Letters*, vol. 42, no. 6, pp. 863–866, Jun. 2021, doi: 10.1109/LED.2021.3072915.

[74] R. Brederlow, W. Weber, C. Dahl, D. Schmitt-Landsiedel, and R. Thewes, “Low-frequency noise of integrated poly-silicon resistors,” *IEEE Trans Electron Devices*, vol. 48, no. 6, pp. 1180–1187, Jun. 2001, doi: 10.1109/16.925245.

[75] G. Ghibaudo, “ON THE THEORY OF CARRIER NUMBER FLUCTUATIONS IN MOS DEVICES,” 1989.

[76] N. K. Rajan, D. A. Routenberg, J. Chen, and M. A. Reed, “1/f noise of silicon nanowire BioFETs,” *IEEE Electron Device Letters*, vol. 31, no. 6, pp. 615–617, Jun. 2010, doi: 10.1109/LED.2010.2047000.

[77] W. Shin *et al.*, “In-memory-computed Low-frequency noise spectroscopy for selective gas detection using a reducible metal oxide,” *Advanced Science*, 2022.

[78] E. Simoen, B. Kaczer, M. Toledano-Luque, and C. Claeys, “(Invited) Random Telegraph Noise: From a Device Physicist’s Dream to a Designer’s Nightmare,” *ECS Trans*, vol. 39, no. 1, pp. 3–15, Sep. 2011, doi: 10.1149/1.3615171.

[79] S. Rumyantsev, G. Liu, M. S. Shur, R. A. Potyrailo, and A. A. Balandin, “Selective gas sensing with a single pristine graphene transistor,” *Nano Lett*, vol. 12, no. 5, pp. 2294–2298, May 2012, doi: 10.1021/nl3001293.

[80] F. Allegrini and A. C. Olivieri, “IUPAC-consistent approach to the limit of detection in partial least-squares calibration,” *Anal Chem*, vol. 86, no. 15, pp. 7858–7866, Aug. 2014, doi: 10.1021/ac501786u.

[81] W. Shin *et al.*, "Proposition of deposition and bias conditions for optimal signal-to-noise-ratio in resistor- And FET-type gas sensors," *Nanoscale*, vol. 12, no. 38, pp. 19768–19775, Oct. 2020, doi: 10.1039/d0nr04406g.

[82] G. Liu, S. Rumyantsev, M. S. Shur, and A. A. Balandin, "Origin of 1/f noise in graphene multilayers: Surface vs. volume," *Appl Phys Lett*, vol. 102, no. 9, Mar. 2013, doi: 10.1063/1.4794843.

[83] W. Shin *et al.*, "Optimization of channel structure and bias condition for signal-to-noise ratio improvement in Si-based FET-type gas sensor with horizontal floating-gate," *Sens Actuators B Chem*, vol. 357, Apr. 2022, doi: 10.1016/j.snb.2022.131398.

초 록

실내외 공기 질, 산업용 가스 누출 및 의료 진단에 대한 관심과 필요가 증가함에 따라 고성능 가스 센서에 대한 수요가 증가하고 있다. 이에 따라 다양한 가스 센서의 종류가 연구되고 있으며, 그 중 반도체 기반 가스 센서는 우수한 성능과 함께 다양한 어플리케이션에 성공적으로 활용되고 있다. 대부분의 선행 연구에서는 반도체 기반 가스 센서의 감지 물질 구조를 나노 구조로 변형하거나 촉매를 도핑함으로써 검출 가스에 대한 충분한 반응성 및 민감성을 향상시키는 데 집중해왔다. 그러나 반도체 기반 가스 센서의 저주파 노이즈 특성에 대한 분석은 부족한 상황이다. 본 논문에서는 수평형 플로팅 게이트를 가지는 전계 효과 트랜지스터(HFGFET)형 가스 센서의 저주파 노이즈 특성을 분석한다. 센서의 플랫폼으로 채택된 HFGFET는 컨트롤 게이트와 플로팅 게이트가 수평으로 마주보고 있으며, 그 위에 감지 물질이 증착되는 구조를 가진다. 본 논문에서는 산화 인듐, 산화 인듐-갈륨-징크, 산화 텅스텐 등의 다양한 감지 물질이 증착된 HFGFET형 센서의 저주파 노이즈를 측정한다. 측정된 결과에 대한 체계적이고 견고한 물리적 분석을 기반으로 HFGFET형 가스 센서의 저주파 노이즈 모델을 제안한다. 제안된 노이즈 모델에 따르면 HFGFET형 가스 센서의 노이즈는 감지 물질과 FET 트랜스듀서의 전하 변동에 의해 결정된다. HFGFET형 센서의 저주파 노이즈가 감지 물질의 전하 변동에 의해 결정될 때 저주파 노이즈 분석을 사용하여 선택적 감지를 실현할 수 있다. 반면 센서의 저주파 노이즈가

FET 트랜스듀서에 의해 결정되는 경우에는 최적의 신호 대 잡음 비를 성취할 수 있는 플랫폼으로 활용될 수 있다. 가스 센서의 저주파 노이즈는 신호 대 잡음 비 개선을 위해 최소화하고 무조건적으로 제거되어야 하는 요소도 아니며 모든 상황에서 선택성을 실현하는 데 사용할 수 있는 만능 감지 특성도 아니다. 필요한 어플리케이션에 따라 저주파 노이즈는 잘 제어되어야 하며, 이 엔지니어링을 가능하게 하려면 저주파 노이즈에 대한 깊은 지식을 갖는 것이 중요하다. 본 논문은 이를 달성할 수 있는 토대를 제공한다.

주요어 : 수평형 플로팅 게이트를 가지는 전계 효과 트랜지스터(HFGFET)형 가스 센서의 저주파 노이즈, 저주파 잡음(LFN), LFN 분광법, 신호 대 잡음비
학번: 2017-20021

List of Publications

Journals

1. ***Wonjun Shin**, *Yujeong Jeong, Mingkyu Kim, Jungsoo Lee, Ryun-Han Koo, Seongbin Hoeng, Gyuweon Jung, Jae-Joon Kim, and Jong-Ho Lee, "Recovery of Off-State Stress-Induced Damage in FET-type Gas Sensor Using Self-Curing Method," Discover Nano, In Press (*Equal Contribution)
2. ***Wonjun Shin**, *Kyung Kyu Min, Jong-Ho Bae, Jaehyeon Kim, Ryun-Han Koo, Dongseok Kwon, Jae-Joon Kim, Daewoong Kwon, and Jong-Ho Lee, "1/*f* noise in synaptic ferroelectric tunnel junction: Impact on convolutional neural network," Advanced Intelligent Systems, In Press (*Equal Contribution)
3. ***Wonjun Shin**, *Ryun-Han Koo, Kyung Kyu Min, Dongseok Kwon, Jae-Joon Kim, Daewoong Kwon, and Jong-Ho Lee, "Unveiling Resistance Switching Mechanisms in Undoped HfO_x Ferroelectric Tunnel Junction Using Low-Frequency Noise Spectroscopy," IEEE Electron Device Letters, In Press (*Equal Contribution)
4. ***Wonjun Shin**, *Jaehyeon Kim, Gyuweon Jung, Suyeon Ju, Sung-Ho Park, Yujeong Jeong, Seongbin Hong, Ryun-Han Koo, Yeongheon Yang, Jae-Joon Kim, Seungwu Han, and Jong-Ho Lee, "In-memory-computed Low-frequency noise spectroscopy for selective gas detection using a reducible metal oxide," Advanced Science, In Press (*Equal Contribution)
5. Jinwoo Park, Seongbin Hong, Yujeong Jeong, Gyuweon Jung, **Wonjun Shin**, Donghee Kim, Chayoung Lee, and Jong-Ho Lee, "H_2S gas sensing properties in polysilicon control-gate FET-type gas sensor," Solid-State Electronics, vol. 200, p. 108543, Feb. 2023.
6. Yujeong Jeong, Seongbin Hong, Gyuweon Jung, **Wonjun Shin**, Chayoung Lee, Jinwoo Park, Donghee Kim, and Jong-Ho Lee, "Effects of oxygen gas in the sputtering process of the WO3 sensing layer on NO_2 sensing

characteristics of the FET-type gas sensor," Solid-State Electronics, vol. 200, p. 108543, Feb. 2023.

7. Seongbin Hong, Yujeong Jeong, Gyuweon Jung, **Wonjun Shin**, Jinwoo Park, Donghee Kim, and Jong-Ho Lee, "Macroscopic Analysis and Design of Si HFGFET Gas Sensor for Sensitive Gas Detection," Solid-State Electronics, vol. 200, p. 108543, Feb. 2023.
8. *Ryun-Han Koo, ***Wonjun Shin**, Kyung Kyu Min, Dongseok Kwon, Jae-Joon Kim, Daewoong Kwon, and Jong-Ho Lee, "Effect of Carrier Transport Process on Tunneling Electroresistance in Ferroelectric Tunnel Junction," IEEE Electron Device Letters, vol. 44, no.1, pp. 164-167, Jan. 2023. (*Equal Contribution)
9. *Gyuweon Jung, *Seongbin Hong, **Wonjun Shin**, Yujeong Jeong, Jinwoo Park, Donghee Kim, and Jong-Ho Lee, "Design Optimization of FET-type Gas Sensor Considering Device Characteristics, Sensitivity, Power, Noise, and SNR," Sensors and Actuators B: Chemical, vol. 369, p. 132257, Oct. 2022. (*Equal Contribution)
10. **Wonjun Shin**, Jong-Ho Bae, Jaehyeon Kim, Ryun-Han Koo, Jae-Joon Kim, Daewoong Kwon, and Jong-Ho Lee, "Variability analysis of ferroelectric FETs in program operation using low-frequency noise spectroscopy," Applied Physics Letters, vol. 121, p. 163501, Sep. 2022.
11. ***Wonjun Shin**, *Yujeong Jeong, Seongbin Hong, Gyuweon Jung, Jinwoo Park, Donghee Kim, Byung-Gook Park, and Jong-Ho Lee, "Fully Integrated FET-type Gas Sensor with Optimized Signal-to-Noise Ratio for H2S Gas Detection," Sensors and Actuators B: Chemical, vol. 367, p. 132052, Sep. 2022. (*Equal Contribution)
12. ***Wonjun Shin**, *Ryun-Han Koo, Seongbin Hong, Dongseok Kwon, Joon Hwang, Byung-Gook Park, and Jong-Ho Lee, "Highly Efficient Self-Curing Method in MOSFET Using Parasitic Bipolar Junction Transistor," IEEE Electron Device Letters, vol. 43, no. 7, pp. 1001-1004, Jul. 2022. (*Equal Contribution)

13. *__Wonjun Shin__, *Jiyoung Yim, Jong-Ho Bae, Jung-Kyu Lee, Seongbin Hong, Jaehyeon Kim, Yujeong Jeong, Dongseok Kwon, Ryun-Han Koo, Gyuweon Jung, Changhyeon Han, Jeonghan Kim, Byung-Gook Park, Daewoong Kwon, and Jong-Ho Lee, "Synergistic Improvement of Sensing Performance in Ferroelectric Transistor Gas Sensors Using Remnant Polarization," Materials Horizons, vol. 9, no. 6, pp. 1623-1630, Jun. 2022. (*Equal Contribution) **[Published as Front Cover]**
14. Jinwoo Park, Gyuweon Jung, Seongbin Hong, Yujeong Jeong, **Wonjun Shin**, Donghee Kim, Chayoung Lee, and Jong-Ho Lee, "Analysis of Cr/Au Contact Reliability in Embedded Poly-Si Micro-heater for FET-type Gas Sensor," Sensors and Actuators B: Chemical, vol. 360, p. 131673, Jun. 2022.
15. **Wonjun Shin**, Jong-Ho Bae, Dongseok Kwon, Ryun-Han Koo, Byung-Gook Park, and Jong-Ho Lee, "Investigation of Low-Frequency Noise Characteristics of Ferroelectric Tunnel Junction: From Conduction Mechanism and Scaling Perspectives," IEEE Electron Device Letters, vol. 43, no. 6, p. 958, Jun. 2022.
16. **Wonjun Shin**, Seongbin Hong, Yujeong Jeong, Gyuweon Jung, Byung-Gook Park, and Jong-Ho Lee, "Effects of Postdeposition Annealing Ambience on NO2 Gas Sensing Performance in Si-Based FET-Type Gas Sensor," IEEE Transactions on Electron Devices, vol. 69, no. 5, pp. 2604-2610, May 2022.
17. Gyuweon Jung, Seongbin Hong, Yujeong Jeong, **Wonjun Shin**, Jinwoo Park, Donghee Kim, and Jong-Ho Lee, "Highly Selective and Low-Power Carbon Monoxide Gas Sensor Based on the Chain Reaction of Oxygen and Carbon Monoxide to WO_3," ACS Applied Materials & Interfaces, vol. 14, no. 15, pp. 17950-17958, Apr. 2022.
18. Donghee Kim, **Wonjun Shin**, Seongbin Hong, Yujeong Jeong, Gyuweon Jung, Jinwoo Park, and Jong-Ho Lee, "Effects of Electrode Structure on H2S Sensing and Low-frequency Noise Characteristics in In2O3-based

Resistor-type Gas Sensors," IEEE Sensors Journal, vol. 22, no. 7, pp. 6311-6320, Apr. 2022.

19. *Wonjun Shin,* *Gyuweon Jung, Seongbin Hong, Yujeong Jeong, Jinwoo Park, Donghee Kim, Byung-Gook Park, and Jong-Ho Lee, "Optimization of Channel Structure and Bias Condition for Signal-to-Noise Ratio Improvement in Si-based FET-type Gas sensor with Horizontal Floating-Gate," Sensors and Actuators B: Chemical, vol. 357, p. 131398, Apr. 2022. (*Equal Contribution)
20. **Wonjun Shin**, Seongbin Hong, Yujeong Jeong, Gyuweon Jung, Jinwoo Park, Donghee Kim, Byung-Gook Park, and Jong-Ho Lee, "Effects of Channel Length Scaling on the Signal-to-Noise Ratio in FET-Type Gas Sensor with Horizontal Floating-Gate," IEEE Electron Device Letters, vol. 43, no. 3, pp. 442-445, Mar. 2022.
21. ***Wonjun Shin**, *Kyung Kyu Min, *Jong-Ho Bae, Jiyong Yim, Dongseok Kwon, Yeonwoo Kim, Junsu Yoo, Joon Hwang, Byung-Gook Park, Daewoong Kwon, and Jong-Ho Lee, "Comprehensive and accurate analysis of the working principle in ferroelectric tunnel junctions using low-frequency noise spectroscopy," Nanoscale, vol. 14, p. 2177-2185, Feb. 2022. (*Equal Contribution) **[Published as Front Cover]**
22. ***Wonjun Shin**, *Jong-Ho Bae, Sihyun Kim, Kitae Lee, Byung-Gook Park, Daewoong Kwon, and Jong-Ho Lee, "Effects of High-Pressure Annealing on the Low-Frequency Noise Characteristics in Ferroelectric FET," IEEE Electron Device Letters, vol. 43, no. 1, p. 13, Jan. 2022.
23. *Dongseok Kwon, *Gyuweon Jung, **Wonjun Shin**, Yujeong Jeong, Seongbin Hong, Seongbin Oh, Jaehyeon Kim, Jong-Ho Bae, Byung-Gook Park, and Jong-Ho Lee, "Efficient Fusion of Spiking Neural Networks and FET-type Gas Sensors for a Fast and Reliable Artificial Olfactory System," Sensors and Actuators B: Chemical, vol. 345, p. 130419, Oct. 2021.
24. **Wonjun Shin**, Daehee Kwon, Minjeong Ryu, Joowon Kwon, Seongbin Hong, Yujeong Jeong, Gyuweon Jung, Jinwoo Park, Donghee Kim, and Jong-Ho Lee, "Effects of IGZO Film Thickness on H_2S Gas Sensing

Performance: Response, Excessive Recovery, Low-frequency Noise, and Signal-to-Noise Ratio," Sensors and Actuators B: Chemical, vol. 344, p. 130148, Oct. 2021.

25. Yujeong Jeong, Seongbin Hong, Gyuweon Jung, **Wonjun Shin**, Jinwoo Park, Donghee Kim, Yong Seok Choi, Jong-Ho Bae, Byung Hee Hong, and Jong-Ho Lee, "Highly Stable Si MOSFET-type Humidity Sensor with Ink-Jet Printed Graphene Quantum Dots Sensing Layer," Sensors and Actuators B: Chemical, vol. 343, p. 130134, Sep. 2021.
26. *Dongseok Kwon, *Gyuweon Jung, **Wonjun Shin**, Yujeong Jeong, Seongbin Hong, Seongbin Oh, Jong-Ho Bae, Byung-Gook Park, and Jong-Ho Lee, "Low-power and Reliable Gas Sensing System Based on Recurrent Neural Networks," Sensors and Actuators B: Chemical, vol. 340, p. 129258, Aug. 2021. (*Equal Contribution)
27. Huaping Wang, Jianmin Ma, Jun Zhang, Yuezhan Feng, Mani Teja Vijjapu, Saravanan Yuvaraja, Sandeep G Surya, Khaled N Salama, Chengjun Dong, Yude Wang, Qin Kuang, Zamaswazi P Tshabalala, David E Motaung, Xianghong Liu, Junliang Yang, Haitao Fu, Xiaohong Yang, Xizhong An, Shiqiang Zhou, Baoye Zi, Qingju Liu, Mario Urso, Bo Zhang, AA Akande, Arun K Prasad, Chu Manh Hung, Nguyen Van Duy, Nguyen Duc Hoa, Kaidi Wu, Chao Zhang, Rahul Kumar, Mahesh Kumar, Youngjun Kim, Jin Wu, Zixuan Wu, Xing Yang, SA Vanalakar, Jingting Luo, Hao Kan, Min Li, Ho Won Jang, Marcelo Ornaghi Orlandi, Ali Mirzaei, Hyoun Woo Kim, Sang Sub Kim, ASM Iftekhar Uddin, Jing Wang, Yi Xia, Chatchawal Wongchoosuk, Anindya Nag, Subhas Mukhopadhyay, Nupur Saxena, Pragati Kumar, Jing-Shan Do, Jong-Ho Lee, Seongbin Hong, Yujeong Jeong, Gyuweon Jung, **Wonjun Shin**, Jinwoo Park, Mara Bruzzi, Chen Zhu, Rex E Gerald, and Jie Huang, "Gas Sensing Materials Roadmap," Journal of Physics: Condensed Matter, vol. 33, no. 30, p. 303001, Jul. 2021.
28. Gyuweon Jung, Seongbin Hong, Yujeong Jeong, **Wonjun Shin**, Jinwoo Park, Donghee Kim, Jong-Ho Bae, Byung-Gook Park, and Jong-Ho Lee, "Response Comparison of Resistor-and Si FET-Type Gas Sensors on the

Same Substrate," IEEE Transactions on Electron Devices, vol. 68, no. 7, pp.3552-3557, Jul. 2021.

29. **Wonjun Shin**, Seongbin Hong, Yujeong Jeong, Gyuweon Jung, Jinwoo Park, Donghee Kim, Byung-Gook Park, and Jong-Ho Lee, "Optimization of Post-Deposition Annealing Temperature for Improved Signal-to-Noise Ratio in In2O3 Gas Sensor," Semiconductor Science and Technology, vol. 36, no. 7, p. 075007, Jul. 2021.
30. ***Wonjun Shin**, *Dongseok Kwon, Jong-Ho Bae, Suhwan Lim, Byung-Gook Park, and Jong-Ho Lee, "Impacts of Program/Erase Cycling on the Low-Frequency Noise Characteristics of Reconfigurable Gated Schottky Diodes," IEEE Electron Device Letters, vol. 42, no. 6, p.863, Jun. 2021. (*Equal Contribution)
31. *Gyuweon Jung, ***Wonjun Shin**, Seongbin Hong, Yujeong Jeong, Jinwoo Park, Donghee Kim, Jong-Ho Bae, Byung-Gook Park, and Jong-Ho Lee, "Comparison of the Characteristics of Semiconductor Gas Sensors with Different Transducers Fabricated on the Same Substrate," Sensors and Actuators B: Chemical, vol. 335, p. 129661, May 2021. (*Equal Contribution)
32. Gyuweon Jung, Yoonki Hong, Seongbin Hong, Dongkyu Jang, Yujeong Jeong, **Wonjun Shin**, Jinwoo Park, Donghee Kim, Chan Bae Jeong, Dong Uk Kim, Ki Soo Chang, and Jong-Ho Lee, "A Low-power Embedded Poly-Si Micro-heater for Gas Sensor Platform Based on a FET Transducer and Its Application for NO2 Sensing, Sensors and Actuators B: Chemical, vol. 334, p. 129642, May 2021.
33. **Wonjun Shin**, Seongbin Hong, Yujeong Jeong, Gyuweon Jung, Jinwoo Park, Donghee Kim, Chayoung Lee, Byung-Gook Park, and Jong-Ho Lee, "Effect of Charge Storage Engineering on the NO2 Gas Sensing Properties of a WO3 FET-type Gas Sensor with a Horizontal Floating-Gate," Nanoscale, vol. 13, no. 19, pp. 9009-9017, May 2021.
34. *Seongbin Hong, *Meile Wu, *Yoonki Hong, Yujeong Jeong, Gyuweon Jung, **Wonjun Shin**, Jinwoo Park, Donghee Kim, Dongkyu Jang, and

Jong-Ho Lee, “FET-type Gas Sensors: A Review,” Sensors and Actuators B: Chemical, vol. 330, p. 129240, Mar. 2021. (*Equal Contribution)

35. *Dongseok Kwon, ***Wonjun Shin**, Jong-Ho Bae, Suhwan Lim, Byung-Gook Park, Jong-Ho Lee, “Investigation of Low-Frequency Noise Characteristics in Gated Schottky Diodes,” IEEE Electron Device Letters, vol. 42, no.3, p. 442, Mar. 2021. (*Equal Contribution)
36. **Wonjun Shin**, Seongbin Hong, Gyuweon Jung, Yujeong Jeong, Jinwoo Park, Donghee Kim, Dongkyu Jang, Byung-Gook Park, and Jong-Ho Lee, “Improved Signal-to-Noise-Ratio of FET-type Gas Sensors using Body Bias Control and Embedded Micro-heater,” Sensors and Actuators B: Chemical, vol. 329, p. 129166, Feb. 2021.
37. ***Wonjun Shin**, *Gyuweon Jung, Seongbin Hong, Yujeong Jeong, Jinwoo Park, Donghee Kim, Dongkyu Jang, Dongseok Kwon, Jong-Ho Bae, Byung-Gook Park, and Jong-Ho Lee, “Proposition of Deposition and Bias Conditions for Optimal Signal-to-Noise-Ratio in Resistor- and FET-type Gas Sensors,” Nanoscale, vol. 12, no. 38, Oct. 2020. (*Equal Contribution)
38. ***Wonjun Shin**, *Gyuweon Jung, Seongbin Hong, Yujeong Jeong, Jinwoo Park, Dongkyu Jang, Byung-Gook Park, and Jong-Ho Lee, “Low Frequency Noise Characteristics of Resistor- and Si MOSFET-type Gas Sensors Fabricated on the Same Si Wafer with In2O3 Sensing Layer,” Sensors and Actuators B: Chemical, vol. 318, p. 128087, Sep. 2020. (*Equal Contribution)
39. Gyuweon Jung, Yujeong Jeong, Yoonki Hong, Meile Wu, Seongbin Hong, **Wonjun Shin**, Jinwoo Park, Dongkyu Jang, and Jong-Ho Lee, “SO2 Gas Sensing Characteristics of FET- and Resistor-type Gas Sensors Having WO3 as Sensing Material,” Solid-State Electronics, vol. 165, p. 107747, Mar. 2020.
40. Yujeong Jeong, Seongbin Hong, Gyuweon Jung, Dongkyu Jang, **Wonjun Shin**, Jinwoo Park, Seung-Ik Han, Hyungtak Seo, and Jong-Ho Lee, “NO2 Sensing Characteristics of Si MOSFET Gas Sensor Based on Thickness of

WO3 Sensing Layer," Journal of Sensor Science and Technology, vol. 29, no. 1, pp. 14-18, Jan. 2020.

Conferences

1. Kangwook Choi, Gyuweon Jung, Seongbin Hong, Yujeong Jeong, **Wonjun Shin**, Jinwoo Park, Chayong Lee, Donghee Kim, and Jong-Ho Lee, "Response Analysis of Resistor-Type Gas Sensor with Bias Voltage Condition," *2022 International Symposium on Olfaction and Electronic Nose (ISOEN)*, May 2022.
2. Gyuweon Jung, Jaehyeon Kim, **Wonjun Shin**, Seongbin Hong, Yujeong Jeong, Jinwoo Park, Donghee Kim, Kangwook Choi, and Jong-Ho Lee, "Optimal Bias Conditions for FET-Type Gas Sensors to Minimize Current Fluctuations," *2022 International Symposium on Olfaction and Electronic Nose (ISOEN)*, May 2022.
3. **Wonjun Shin**, Seongbin Hong, Yujeong Jeong, Gyuweon Jung, Byung-Gook Park, and Jong-Ho Lee, "Highly Improved NO_2 Gas Sensing Performances Using Charge Storage Engineering in FET-type Gas Sensor with Embedded Micro-heater," *2022 Spring Conference of the Korean Sensors Society*, Apr. 2022.
4. Yujeong Jeong, Seongbin Hong, Gyuweon Jung, **Wonjun Shin**, Byung-Gook Park, and Jong-Ho Lee, "Comparison of the H_2S Sensing Characteristics of the Amplifier Circuits Consisting of the FET-type Gas Sensors with Different Load," *2022 Spring Conference of the Korean Sensors Society*, Apr. 2022.
5. Seongbin Hong, Yujeong Jeong, Gyuweon Jung, **Wonjun Shin**, Jinwoo Park, Donghee Kim, Chayoung Lee, Kangwook Choi, Jun Shik Kim, Cheol Seong Hwang, and Jong-Ho Lee, "Capacitor-Based Gas Sensor with a ZnO Sensing Layer," *The 29th Korean Conference on Semiconductors (KCS)*, Jan. 2022.
6. Jinwoo Park, Seongbin Hong, Yujeong Jeong, Gyuweon Jung, **Wonjun Shin**, Donghee Kim, Chayoung Lee, and Jong-Ho Lee, "Effects of

Annealing Temperature on Stability of FET-type Gas Sensor," *The 29th Korean Conference on Semiconductors (KCS)*, Jan. 2022.

7. Kangwook Choi, Gyuweon Jung, Seongbin Hong, Yujeong Jeong, **Wonjun Shin**, Jinwoo Park, Donghee Kim, Jong-Ho Bae, Byung-Gook Park, and Jong-Ho Lee, "Response Analysis of Resistor-type Gas Sensor with Read Bias Condition," *The 29th Korean Conference on Semiconductors (KCS)*, Jan. 2022.

8. Seongbin Hong, Yujeong Jeong, Gyuweon Jung, **Wonjun Shin**, Jinwoo Park, Donghee Kim, Chayoung Lee, Kangwook Choi, and Jong-Ho Lee, "Long-term Degradation Characteristics of Gas Response depending on Deposition Atmosphere of Sensing Layer in FET-type Gas Sensors," *2021 Fall Conference of the Korean Sensors Society*, Oct. 2021.

9. Yujeong Jeong, Seongbin Hong, Gyuweon Jung, **Wonjun Shin**, Chayoung Lee, Jinwoo Park, Donghee Kim, Kangwook Choi, and Jong-Ho Lee, "NO_2 Sensing Characteristics of the Amplifier Circuit Consisting of the FET-type Gas Sensors with FET Load," *2021 Fall Conference of the Korean Sensors Society*, Oct. 2021.

10. Seongbin Hong, Yujeong Jeong, Gyuweon Jung, **Wonjun Shin**, Jinwoo Park, Donghee Kim, Chayoung Lee, and Jong-Ho Lee, "Gas Sensing Performance of a Gated Lateral pnp-Bipolar Junction Transistor Gas Sensor Having a Horizontal Floating-Gate Structure," *2021 International Conference on Solid State Devices and Materials (SSDM)*, Sep. 2021.

11. Yujeong Jeong, **Wonjun Shin**, Seongbin Hong, Gyuweon Jung, Chayoung Lee, Jinwoo Park, Donghee Kim, and Jong-Ho Lee, "Amplifier Circuit Consisting of the FET-type Gas Sensors with Tunable FET Load," *2021 International Conference on Solid State Devices and Materials (SSDM)*, Sep. 2021.

12. **Wonjun Shin**, Byeongchan Choi, Junmo Lee, Seongbin Hong, Yujeong Jeong, Gyuweon Jung, Jinwoo Park, Donghee Kim, Chayoung Lee, and

Jong-Ho Lee, “Sub-ppm Detection of NO_2 Gas using IGZO TFT-type Gas Sensor with Optimal Signal-to-Noise Ratio,” *2021 International Conference on Solid State Devices and Materials (SSDM)*, Sep. 2021.

13. **Wonjun Shin**, Byeongchan Choi, Junmo Lee, Seongbin Hong, Yujeong Jeong, Gyuweon Jung, Jinwoo Park, Donghee Kim, Chayoung Lee, and Jong-Ho Lee, “Effects of Oxygen Flow Rate on the NO_2 Gas Sensing and Low-frequency Noise Characteristics in IGZO Gas Sensors,” *The 19th International Nanotech Symposium & Exhibition*, Jul. 2021.
14. Donghee Kim, Jiseong Im, Seongbin Hong, Yujeong Jeong, Gyuweon Jung, **Wonjun Shin**, Jinwoo Park, and Jong-Ho Lee, “A Spiking Neural Network for Time-Efficient Gas Concentration Level Estimation in Resistor-Type Gas Sensors,” *2021 Summer Annual Conference of IEIE*, Jun. 2021.
15. Seongbin Hong, Yujeong Jeong, Gyuweon Jung, **Wonjun Shin**, Jinwoo Park, Donghee Kim, and Jong-Ho Lee, “Macroscopic Analysis and Design of Si HFGFET Gas Sensor for Sensitive Gas Detection,” *The 28th Korean Conference on Semiconductors (KCS)*, Jan. 2021.
16. **Wonjun Shin**, Joowon Kwon, Daehee Kwon, Minjeong Ryu, Seongbin Hong, Yujeong Jeong, Gyuweon Jung, Jinwoo Park, Donghee Kim, and Jong-Ho Lee, “Effect of Post-Deposition Annealing Atmosphere on NO_2 Gas Sensing and Low-frequency Noise in IGZO Thin-film Chemiresistor Gas Sensor,” *The 28th Korean Conference on Semiconductors (KCS)*, Jan. 2021.
17. Yujeong Jeong, Seongbin Hong, Gyuweon Jung, **Wonjun Shin**, Jinwoo Park, Donghee Kim, and Jong-Ho Lee, “Effects of Oxygen Gas Flow on the Response of FET-type Gas Sensor with Sputtered WO_3 Sensing Layer,” *The 28th Korean Conference on Semiconductors (KCS)*, Jan. 2021.
18. Gyuweon Jung, Seongbin Hong, Yujeong Jeong, **Wonjun Shin**, Jinwoo Park, Donghee Kim, Jong-Ho Bae, Byung-Gook Park, and Jong-Ho Lee, “H_2S Gas Sensing Characteristics of Si FET-type Gas Sensor with Localized

Micro-heater," *The 28th Korean Conference on Semiconductors (KCS)*, Jan. 2021.

19. Jinwoo Park, Seongbin Hong, Yujeong Jeong, Gyuweon Jung, **Wonjun Shin**, Donghee Kim, and Jong-Ho Lee, "H_2S Gas Sensing Properties in Polysilicon Control-Gate FET Gas Sensor," *The 28th Korean Conference on Semiconductors (KCS)*, Jan. 2021.
20. Donghee Kim, **Wonjun Shin**, Seongbin Hong, Yujeong Jeong, Gyuweon Jung, Jinwoo Park, and Jong-Ho Lee, "Effect of Sensing Layer Length on H_2S Gas Sensing and Low-frequency Noise in Resistor-type Gas Sensor," *The 28th Korean Conference on Semiconductors (KCS)*, Jan. 2021.
21. **Wonjun Shin**, Seongbin Hong, Yujeong Jeong, Gyuweon Jung, Jinwoo Park, Dongseok Kwon, Dongkyu Jang, Donghee Kim, Byung-Gook Park, and Jong-Ho Lee, "Efficient Improvement of Sensing Performance Using Charge Storage Engineering in Low Noise FET-type Gas Sensors," *2020 IEEE International Electron Devices Meeting (IEDM)*, Dec. 2020.
22. Yujeong Jeong, **Wonjun Shin**, Seongbin Hong, Gyuweon Jung, Jinwoo Park, Dongkyu Jang, Donghee Kim, Dongseok Kwon, Byung-Gook Park, and Jong-Ho Lee, "Highly Sensitive Amplifier Circuit Consisting of Complementary pFET-type and Resistor-type Gas Sensors," *2020 IEEE International Electron Devices Meeting (IEDM)*, Dec. 2020.
23. **Wonjun Shin**, Seongbin Hong, Yujeong Jeong, Gyuweon Jung, Jinwoo Park, Donghee Kim, Byung-Gook Park, and Jong-Ho Lee, "Effect of Post-Deposition Annealing Temperature on H_2S Sensing and Low-Frequency Noise Characteristics of In_2O_3 Gas Sensor," *2020 International Conference on Solid State Devices and Materials (SSDM)*, Sep. 2020.
24. Donghee Kim, **Wonjun Shin**, Seongbin Hong, Yujeong Jeong, Gyuweon Jung, Jinwoo Park, Dongkyu Jang, Byung-Gook Park, and Jong-Ho Lee, "Effect of Bias Condition on the Gas Response in Resistor- and FET-type Gas Sensors," *2020 Summer Annual Conference of IEIE*, Aug. 2020.

25. Jinwoo Park, Gyuweon Jung, Seongbin Hong, Yujeong Jeong, **Wonjun Shin**, Donghee Kim, Byung-Gook Park, and Jong–Ho Lee, "NO_2 Gas Sensing Properties in FET-type Gas Sensor having Horizontal Floating-Gate," *2020 Summer Annual Conference of IEIE*, Aug. 2020.
26. Seongbin Hong, Yujeong Jeong, Gyuweon Jung, **Wonjun Shin**, Jinwoo Park, Jung-Kyu Lee, Dongkyu Jang, and Jong-Ho Lee, "Highly Sensitive and Selective Gas Sensing Performance in MOSFET-Based Gas Sensor Using Facile Metal Nanoparticle Agglomeration Process," *The 27th Korean Conference on Semiconductors (KCS)*, Feb. 2020.
27. Jinwoo Park, Seongbin Hong, Yujeong Jeong, Gyuweon Jung, **Wonjun Shin**, Dongkyu Jang, and Jong-Ho Lee, "Effects of Body Bias and Operation Region on Gas Response in FET-type Gas Sensor having Horizontal Floating-Gate," *The 27th Korean Conference on Semiconductors (KCS)*, Feb. 2020.
28. **Wonjun Shin**, Gyuweon Jung, Seongbin Hong, Yujeong Jeong, Jinwoo Park, Dongkyu Jang, and Jong-Ho Lee, "Effect of Resistor-type Gas Sensor Scaling on Sensing and Low frequency Noise Characteristics," *The 27th Korean Conference on Semiconductors (KCS)*, Feb. 2020.
29. Yujeong Jeong, Seongbin Hong, Gyuweon Jung, Dongkyu Jang, **Wonjun Shin**, Jinwoo Park, Seung-Ik Han, Hyungtak Seo, and Jong-Ho Lee, "Sensing Characteristics of the MOSFET-type Gas Sensor with Sputtered WO_3 Sensing Layer," *The 27th Korean Conference on Semiconductors (KCS)*, Feb. 2020.
30. Dongkyu Jang, Gyuweon Jung, Yujeong Jeong, Yoonki Hong, Seongbin Hong, **Wonjun Shin**, Ki Soo Chang, Chan Bae Jeong, Byung-Gook Park, and Jong-Ho Lee, "Efficient Integration of Si FET-type Gas Sensors and Barometric Pressure Sensors on the Same Substrate," *2019 IEEE International Electron Devices Meeting (IEDM)*, Dec. 2019.
31. Gyuweon Jung, Yoonki Hong, Seongbin Hong, Yujeong Jeong**, Wonjun**

Shin, Jinwoo Park, Jung-Kyu Lee, Dongkyu Jang, and Jong-Ho Lee, “Detection of Low Concentration NO_2 Gas Using Si FET-Type Gas Sensor with Localized Micro-Heater for Low Power Consumption,” *2019 IEEE Sensors*, Oct. 2019.

32. Seongbin Hong, Yujeong Jeong, Yoonki Hong, Gyuweon Jung, **Wonjun Shin**, Jinwoo Park, and Jong-Ho Lee, “A Comparative Study on Gas Sensing Characteristics in Si MOSFET Gas Sensor Platform based on Integrated Sensing Mechanisms,” *2019 Fall Conference of the Korean Sensors Society*, Aug. 2019.

33. Gyuweon Jung, Yoonki Hong, Seongbin Hong, Yujeong Jeong, **Wonjun Shin**, Jinwoo Park, Jungkyu Lee, Dongkyu Jang, and Jong-Ho Lee, “Gas Sensing Characteristics of the Horizontal Floating-Gate FET-type Gas Sensor Deposited with In_2O_3 Film,” *2019 Fall Conference of the Korean Sensors Society*, Aug. 2019.

34. Jong-Ho Lee, Seongbin Hong, Yoonki Hong, Yujeong Jeong, Gyuweon Jung, **Wonjun Shin**, Jinwoo Park, Dongkyu Jang, and Jung-Kyu Lee, “Sensing Mechanisms and Micro-Heater in Gas Sensors,” *2019 IEEE International Conference on Circuits, Systems and Devices (ICCSD)*, Aug. 2019.

35. Jinwoo Park, Yujeong Jeong, Yoonki Hong, Seongbin Hong, Gyuweon Jung, **Wonjun Shin**, Jung-kyu Lee, Byung-Gook Park, and Jong–Ho Lee, “Effect of Body Bias on Gas Response in FET-type Gas Sensor having Horizontal Floating-Gate,” *2019 Summer Annual Conference of IEIE*, Jun. 2019.

36. **Wonjun Shin**, Gyuweon Jung, Yujeong Jeong, Seongbin Hong, Jinwoo Park, Yoonki Hong, Byung-Gook Park, and Jong-Ho Lee, “The Effects of Operating Temperature on Field Effect Transistor Gas Sensor with In_2O_3 Sensing Layer,” *2019 Summer Annual Conference of IEIE*, Jun. 2019.

37. Gyuweon Jung, Hyeongsu Kim, Yujeong Jeong, Yoonki Hong, Meile Wu,

Seongbin Hong, Dongkyu Jang, **Wonjun Shin**, and Jong-Ho Lee, "Accurate Identification of Gas Type and Concentration using DNN Reflecting the Sensing Properties of MOSFET-type Gas Sensor," *2019 International Symposium on Olfaction and Electronic Nose (ISOEN)*, May 2019.

38. Jong-Ho Lee, Yujeong Jeong, Yoonki Hong, Meile Wu, Seongbin Hong, Gyuweon Jung, and **Wonjun Shin**, "High Performance Gas Sensor Platform Based on Integrated Sensing Mechanisms," *2019 International Conference on Semiconductor Technology for Ultra Large Scale Integrated Circuits and Thin Film Transistors (ULSIC vs. TFT 7)*, May 2019.

Patent

1. Jong-Ho Lee, Wonjun Shin, "Charge storage engineering in FET-type gas sensor having floating-gate."
   Korean Patent filed 10-2021-0067172, June 2021
   United States Patent filed 17 736,988, May 2022

Honors

1. Excellent Graduate Student Award, BK21, Feb. 2022.
2. Gold Prize, The 24th Humantech Thesis Contests, Samsung Electronics, Feb. 2022, “Hybrid Training Method for an Accurate Neuromorphic System with an AND Flash Array Architecture”.
3. Commendation for Excellent Student in the BK21 FOUR project, Awarded by Deputy Prime Minister/Ministry of Education, Jan. 2023
4. Silver Prize, The 25th Humantech Thesis Contests, Samsung Electronics, Feb. 2023, “Unveiling the Hidden RRAM in Undoped Hafnium Oxide Ferroelectric Tunnel Junction.”
5. Silver Prize, The 25th Humantech Thesis Contests, Samsung Electronics, Feb. 2023, “Noisy Deep Q-Networks Using Low-Frequency Noise of 3D Flash Memory Array for Efficient Exploration.”